Available online at www.sciencedirect.com
SCIENCE DIRECT®
ELSEVIER
International Journal of Solids and Structures 42 (2005) 5615–5655
INTERNATIONAL JOURNAL OF SOLIDS and STRUCTURES
www.elsevier.com/locate/ijsolstr

Thermomechanical modeling of metals at finite strains: First and mixed order finite elements

Laurent Adam *, Jean-Philippe Ponthot [1]

LTAS – Milieux Continus et Thermomécanique, Université de Liège, 1, Chemin des Chevreuils, B-4000 Liège-1, Belgium

Received 11 January 2005
Available online 19 April 2005

Abstract

The aim of this paper is to describe an updated EAS (Enhanced Assumed Strain) finite element formalism developed to model the thermomechanical behavior of metals submitted to large strains. We will also expose the use of mixed order elements (first order mechanical elements strongly coupled with quadratic thermal elements) which, as we will show, is of particular interest for modeling fast processes inducing important temperature gradients. The features of this formalism, used jointly with an Updated Lagrangian approach and an hypoelastic anisothermal constitutive formulation, will be described. Three applications involving finite strains and important thermomechanical couplings will be studied. The results obtained will be compared with the results given by the now classical SRI (Selective Reduced Integration) formalism.

Keywords: Finite element; Mixed order element; Large strains; Enhanced assumed strain; Selective reduced integration; Linear element; Quadratic element

1. Introduction

The use of first order elements for the numerical modeling of metal forming or impact processes has become a standard even more if contact interactions between bodies need to be managed. Indeed, these elements have the advantages of being simpler, and less sensitive to high distortions than higher order elements. Even more, numerical methods acting on mesh such as ALE, remeshing,... are easier to handle

* Corresponding author. Present Address: e-Xstream Engineering S.A., Avenue G. Lemaître, 4, B-1348 Louvain-la-Neuve, Belgium. Tel.: +32 10 478031; fax: +32 10 472180.
E-mail addresses: laurent.adam@e-xstream.com (L. Adam), jp.ponthot@ulg.ac.be (J.-P. Ponthot).
[1] Tel.: +32 4 3669310; fax: +32 4 3669141.

0020-7683/$ - see front matter
doi:10.1016/j.ijsolstr.2005.03.020

with such linear elements. However, standard mechanical first order elements are subject to locking both for shear and volumetric deformation (Bathe, 1996; Zienkiewicz and Taylor, 1994).

One of the most classical way to overcome locking is to under integrate the element (Malkus and Hughes, 1978; Brezzi and Fortin, 1991). However, under integrating the elements can give rise to mesh instabilities also known as hourglass modes. Selective Reduced Integration (SRI) (see Malkus and Hughes, 1978; Ponthot, 1995) is one of the most implemented finite element formalism. It enables to selectively under integrate the shear or volume strains to avoid, or almost suppress, the shear or volumetric locking. Amongst these two choices, the most commonly used is to under integrate the volumetric strains. In that case, only shear locking remains thus allowing poor results when the bending response is of major importance. The use of a fine mesh can then help to decrease the locking effect that remains. In addition to locking phenomena, SRI formalism results in elements that do not pass the patch test and that can develop hourglassing (Simo and Rifai, 1990; Bathe, 1996). However, in the Updated Lagrangian framework described in the following, hourglassing hardly appears except when fully reduced integration is used (Flanagan and Belytschko, 1981) which will not be the case here.

Another way to overcome locking is to add internal, lacking modes of deformation to the element. Here we will use an element enhancement based on the Enhanced Assumed Strain (EAS) formalism initiated by Simo et al. (Simo and Rifai, 1990; Simo and Armero, 1992; Simo et al., 1993). This formalism enables to obtain (almost) locking-free elements which have good coarse mesh accuracy and which pass the patch test (Simo et al., 1993). The mesh instabilities, appearing under compressive loads, initially present in the formulation of Simo et al. (Simo and Rifai, 1990; Simo and Armero, 1992) are here suppressed following the work of Glaser and Armero (1997). However, hourglassing can still develop under extreme tensile conditions (Glaser and Armero, 1997; de Souza Neto and Peric, 1995). Let us note that these mesh instabilities can vanish if a stabilization techniques is used, or if a finer integration procedure is used at the element level (Simo et al., 1993; Glaser and Armero, 1997; Roehl and Ramm, 1996; Wall et al., 2000; Reese et al., 2000; Hansbo, 1998). However, it does not exist a ''natural'' stabilization techniques which does not need to adjust a control parameter which has, or not, a physical and/or numerical meaning (see Glaser and Armero (1997) for example). In our case, these instabilities, as for the SRI formalism, hardly appear so that no stabilization technique is actually needed in the strain range of interest.

One of the main interest of the EAS formalism is that it is also strain-driven (as for standard or SRI elements) so that the constitutive models and integration schemes do not need to be modified. On the other hand a drawback of EAS elements is to increase the CPU cost and memory usage for a given model. As we will see in the sequel, the local resolution scheme that we use for the EAS modes enables us to almost suppress the increase in memory storage, the CPU cost increase being rather small for large models.

EAS finite element formalism are usually developed for total Lagrangian formulations and not in the context of Updated Lagrangian formulations. Hyperelastic constitutive formalism has also become more widespread than hypoelastic formalism (Simo, 1985; Simo and Miehe, 1992 Lehmann, 1984; Lemaitre and Chaboche, 1985; Lion, 2000; Ibrahimbegovic and Chorfi, 2002; Svendsen et al., 1998; Weber and Anand, 1990; Arif et al., 2000). Here we will expose an updated EAS formalism in an Updated Lagrangian framework using hypoelastic constitutive laws.

We will also couple first order mechanical elements (SRI or EAS elements) to linear and quadratic thermal elements giving rise to mixed order elements. Thus, mechanical and/or thermal solutions on coarse meshes can be improved by the use of the EAS formalism and/or quadratic thermal finite elements. We will also compare the behavior of such elements to first order SRI thermomechanical elements and demonstrate the benefits that results from the use of such a mixed formulation.

The paper is sectioned as followed: The next section will briefly expose the anisothermal finite strain framework. Section 3 will show how the updated EAS formulation is used to remove the shear and volumetric locking developed by classical, fully integrated, first order elements. Section 4 will describe how mechanical and thermal elements are strongly coupled, and how the thermomechanical couplings are managed.

Section 5 will expose the integration procedure of the momentum and heat equations at the structural level, as well as the integration of the constitutive laws at the element level. Section 6 will then expose the results obtained for three applications involving finite strains. Finally, Section 7 will hold the conclusions.

2. Anisothermal large deformation framework

2.1. Finite strains kinematics

Let us consider two configurations of a body: first, the reference configuration (not necessarily the initial configuration) at a certain time t_0 where the position of a material particle at this time is denoted by its *position vector* $\boldsymbol{X}$ and second, the current configuration, at time t, where the position of the same material particle is $\boldsymbol{x}$. Then there exists a one-to-one mapping between $\boldsymbol{x}$ and $\boldsymbol{X}$ of the form

$$\boldsymbol{x} = \boldsymbol{x}(\boldsymbol{X}, t) \tag{1}$$

The *velocity* of the reference point $\boldsymbol{X}$ is the material time derivative of the position vector and is defined by

$$\boldsymbol{v} = \dot{\boldsymbol{x}} = \frac{\partial \boldsymbol{x}(\boldsymbol{X}, t)}{\partial t} \tag{2}$$

The *deformation gradient* of the motion at $\boldsymbol{X}$ is the second-rank two-point tensor $\boldsymbol{F}$ such that

$$\boldsymbol{F} = \frac{\partial \boldsymbol{x}}{\partial \boldsymbol{X}} \quad \text{with } J = \det \boldsymbol{F} > 0 \tag{3}$$

By the polar decomposition, we can uniquely decompose $\boldsymbol{F}$ as

$$\boldsymbol{F} = \boldsymbol{R}\boldsymbol{U} \quad \text{with } \boldsymbol{R}^{\mathrm{T}}\boldsymbol{R} = \boldsymbol{I} \quad \text{and} \quad \boldsymbol{U} = \boldsymbol{U}^{\mathrm{T}} \tag{4}$$

The corresponding *spatial gradient of velocity* is given by

$$\boldsymbol{L} = \frac{\partial \boldsymbol{v}}{\partial \boldsymbol{x}} = \dot{\boldsymbol{F}}\boldsymbol{F}^{-1} \tag{5}$$

It can be decomposed into its symmetric and the antisymmetric parts, $\boldsymbol{L} = \boldsymbol{D} + \boldsymbol{W}$ with

$$\boldsymbol{D} = \frac{1}{2}(\boldsymbol{L} + \boldsymbol{L}^{\mathrm{T}}) \text{ the rate of deformation} \tag{6}$$

$$\boldsymbol{W} = \frac{1}{2}(\boldsymbol{L} - \boldsymbol{L}^{\mathrm{T}}) \text{ the spin tensor} \tag{7}$$

2.2. Conservation equations

In this section, we will briefly formulate the fundamental set of conservation equations of a thermomechanical formulation.

2.2.1. Mechanical part

The equations used in this part of the formulation are the classical, and well known, conservation equations of the mass and momentum (see e.g. Malvern, 1969).

The mass conservation equation: The equation is used in its classical form, given by

$$\frac{\partial \rho}{\partial t} + \rho \operatorname{div} \boldsymbol{v} = 0 \tag{8}$$

where ρ is the density which can be expressed in terms of the initial density ρ_0 by

$$\rho = \frac{\rho_0}{J} \tag{9}$$

The momentum conservation equation: Using the above equation, the principle of conservation of the momentum leads to

$$\rho \frac{\partial \boldsymbol{v}}{\partial t} = \rho \boldsymbol{b} + \operatorname{div} \boldsymbol{\sigma} \tag{10}$$

where $\boldsymbol{b}$ is the body force vector expressed per unit of mass, and $\boldsymbol{\sigma}$ is the Cauchy stress tensor. Using the equation of conservation of the angular momentum, it is easy to show that $\boldsymbol{\sigma}$ is a symmetric tensor.

2.2.2. Thermal part

The equation of heat is derived from the first principle of thermodynamics (conservation of energy). We have assumed, given a certain choice of state variables and a model for the description of the kinematics of the body, to express that equation as (see Simo and Miehe, 1992; Adam, 2003 for more details)

$$\rho c_v \dot{T} = \dot{W}^{\text{thel}} - \rho \frac{\partial}{\partial \boldsymbol{\alpha}} \left[\psi - T \frac{\partial \psi}{\partial T} \right] \cdot \dot{\boldsymbol{\alpha}} + \dot{W}^{\text{irr}} + \rho r - \operatorname{div} \boldsymbol{q} \tag{11}$$

where c_v is the specific heat at constant volume, T is the temperature, $\dot{W}^{\text{thel}}$ is the thermoelastic structural heating, ψ is the Helmholtz's free energy, $\boldsymbol{\alpha}$ is the vector of internal state variables, $\dot{W}^{\text{irr}}$ is the plastic dissipation term, r is the heat source and $\boldsymbol{q}$ is the thermal flux linked to the temperature gradient by the well known Fourier's law. In complement to the vector of internal variables $\boldsymbol{\alpha}$, our choice of state variables is $[\boldsymbol{\epsilon}^{\text{rev}}, T]$ where $\boldsymbol{\epsilon}^{\text{rev}}$ is a representative tensor of the reversible part of the deformation, thus we have $\psi = \psi(\boldsymbol{\epsilon}^{\text{rev}}, T, \boldsymbol{\alpha})$. As we will use an hypoelastic approach, $\boldsymbol{\epsilon}^{\text{rev}}$ will never appear explicitly in the equations and so we do not have to define it explicitly. In the following, we will use plastic models involving only isotropic hardening so that $\boldsymbol{\alpha}$will contain only a scalar variable related to the accumulated plastic strains (note that kinematic hardening can be easily introduced in the present internal variables formulation—see Adam (2003)).

2.3. Constitutive equations

2.3.1. General formulation

It is generally assumed, see e.g. Whertheimer (1982) and Wriggers et al. (1989) for details, that the rate of deformation can be additively decomposed into an elastic (reversible), an inelastic (irreversible) and a thermal parts, i.e. $\boldsymbol{D} = \boldsymbol{D}^{\text{e}} + \boldsymbol{D}^{\text{p}} + \boldsymbol{D}^{\text{th}}$ and that the hypoelastic stress–strain relation is given, for elasto-plastic materials, by a relation of the type

$$\overset{\triangledown}{\boldsymbol{\sigma}} = \mathscr{H}(T) : (\boldsymbol{D} - \boldsymbol{D}^{\text{p}} - \boldsymbol{D}^{\text{th}}) + \dot{\mathscr{H}}(T) : ((\mathscr{H}(T))^{-1} : \boldsymbol{\sigma}) \tag{12}$$

where $\mathscr{H}(T)$ is the Hooke stress–strain tensor at temperature T given by

$$\mathscr{H}(T)_{ijkl} = K(T)\delta_{ij}\delta_{kl} + 2G(T)\left(\delta_{ik}\delta_{jl} - \frac{1}{3}\delta_{ij}\delta_{kl}\right) \tag{13}$$

in which: $\overset{\triangledown}{\boldsymbol{\sigma}}$ is an objective rate of Cauchy stress tensor; $\boldsymbol{D}$ is the rate of deformation; $\boldsymbol{D}^{\text{p}}$ is the plastic part of $\boldsymbol{D}$; $\boldsymbol{D}^{\text{e}}$ is the elastic part of $\boldsymbol{D}$; $\boldsymbol{D}^{\text{th}}$ is the thermal part of $\boldsymbol{D}$; $\boldsymbol{\delta}$ is the Kronecker delta symbol; $K(T)$ is the bulk modulus of the material at T; $G(T)$ is the shear modulus of the material at T.

$K(T)$ and $G(T)$ can also be expressed in terms of the Young's modulus $E(T)$ and Poisson's ratio $v(T)$ as

$$K(T) = \frac{E(T)}{3(1-2v(T))} \quad \text{and} \quad G(T) = \frac{E(T)}{2(1+v(T))} \tag{14}$$

Classically, for a $J2$ elasto-plastic von Mises material with isotropic hardening, we assume the existence of a *yield function* f given by

$$f(\boldsymbol{\sigma}, \bar{\epsilon}^{\mathrm{p}}, T) = \bar{\sigma} - \sigma^{\mathrm{v}}(\bar{\epsilon}^{\mathrm{p}}, T) = 0 \tag{15}$$

where $\bar{\sigma}$ is the effective stress, i.e. $\bar{\sigma} = \sqrt{\frac{3}{2}\boldsymbol{s} : \boldsymbol{s}}$; $\boldsymbol{s}$ is the deviator of the stress tensor; $\sigma^{\mathrm{v}}(\bar{\epsilon}^{\mathrm{p}}, T)$ is the current yield stress; $\bar{\epsilon}^{\mathrm{p}}$ is the effective plastic strain.

Finally, the pressure p is given by

$$p = \frac{1}{3}\mathrm{tr}(\boldsymbol{\sigma}) \tag{16}$$

2.3.2. Flow rule

When plastic deformation occurs one can write, in the case of associative plasticity

$$\boldsymbol{D}^{\mathrm{p}} = \Lambda \boldsymbol{N} \quad \text{where } \boldsymbol{N} = \frac{\partial_{\sigma} f}{\|\partial_{\sigma} f\|} \tag{17}$$

is the unit outward normal ($\boldsymbol{N}:\boldsymbol{N} = 1$) to the yield surface f and Λ is a positive parameter called the *consistency parameter* (which can be determined by the so-called consistency condition i.e. $\dot{f} = 0$).

2.3.3. Isotropic hardening law

The evolution equation of σ^{v} is given by

$$\dot{\sigma}^{\mathrm{v}} = \sqrt{\frac{2}{3}} g(T) \Lambda \tag{18}$$

where $g(T)$ is called the *plastic modulus* and corresponds to the slope of the effective stress vs. effective plastic strain curve under uniaxial loading conditions. Generally, g is a function of the effective plastic strain (which in this case of isotropic hardening is the only internal variable), leading to a non-linear evolution equation for σ^{v}. Eq. (18) can also be rewritten, in this more general case, as

$$\dot{\sigma}^{\mathrm{v}} = g(T, \bar{\epsilon}^{\mathrm{p}}) \dot{\bar{\epsilon}}^{\mathrm{p}} \tag{19}$$

where $\dot{\bar{\epsilon}}^{\mathrm{p}}$ is the rate of effective plastic strain defined as

$$\dot{\bar{\epsilon}}^{\mathrm{p}} = \sqrt{\frac{2}{3}} \boldsymbol{D}^{\mathrm{p}} : \boldsymbol{D}^{\mathrm{p}} = \sqrt{\frac{2}{3}} \Lambda \tag{20}$$

2.3.4. Thermal part

The equation governing the evolution of the thermal part of the tensor of the rate of deformation is a generalization of the equation used in infinitesimal strain theory (Booley and Weiner, 1960) which is given by

$$D_{ij}^{\mathrm{th}} = \beta \dot{T} \delta_{ij} \tag{21}$$

where β is the linear thermal expansion coefficient. Notice that as β is a "local" or "tangent" thermal expansion coefficient, which can vary with temperature, no derivative of β will appear in the constitutive model under consideration (see Adam (2003) for more details).

2.3.5. Thermomechanical couplings

The plastic heating $\dot{W}^{\text{irr}}$ is the most important heating source resulting from a mechanical deformation. As explained in (Chrysochoos, 1987; Chrysochoos and Louche, 2000; Rosakis et al., 2000; Simo and Miehe, 1992) a part of the plastic deformation does not generate heat but induces the storage of energy in the material through the creation of micro-stress fields linked to the development of dislocations and other microscopic defects. That part of non-recoverable energy is expressed by the term

$$\rho \frac{\partial}{\partial \boldsymbol{\alpha}} \left[\psi - T \frac{\partial \psi}{\partial T} \right] \dot{\boldsymbol{\alpha}} \tag{22}$$

in Eq. (11). This term is usually managed by considering that it represents, in metal submitted to large strains, between 5% and 15% of the plastic heating $\dot{W}^{\text{irr}}$. This assumption, suggested by Taylor and Quinney (1937), is used by many researchers in the field of computational mechanics (Simo and Miehe, 1992; Zhou et al., 1996; Camacho and Ortiz, 1997; Wriggers et al., 1989; Tonkovic et al., 2001). So, these two terms can be merged in a unique expression written as $\chi \dot{W}^{\text{irr}}$ where χ is a multiplicative factor, called the Taylor–Quinney factor, which classically takes its value between 0.85 and 0.95 (for the numerical applications we will set χ at 0.9).

In our hypoelastic constitutive models, the plastic heating will be expressed as

$$\dot{W}^{\text{irr}} = \bar{\sigma} \dot{\bar{\epsilon}}^{\text{p}} \tag{23}$$

Notice that so far it does not exist, amongst constitutive models which postulate an expression for the free energy ψ, a thermo-elastoplastic model which gives, for a same set of parameters, physically realistic results for the plastic behavior and for the prediction of the stored and dissipated energies (see Rosakis et al., 2000; Chrysochoos, 1987; Chrysochoos and Louche, 2000).

The thermoelastic heating, represented by the term $\dot{W}^{\text{thel}}$ in Eq. (11), has a minor contribution to the thermal equation, especially in the field of metal forming processes. Many authors have neglected this term but, as a precise analyze can show, it has a stabilizing effect on the solution schemes used in the field of thermo-elastoplastic problems. Indeed Armero and Simo (1992, 1993) have shown that this term has to be integrated properly in the mechanical phase of a staggered scheme in order to have an unconditionally stable algorithm for the resolution of the coupled problem.

In the case of constant elastic properties, it can be expressed (Booley and Weiner, 1960), using some properties of the plastic flow, as

$$\dot{W}^{\text{thel}} = T \frac{\partial \boldsymbol{\sigma}}{\partial T} : \boldsymbol{D}^{\text{rev}} = -3K\beta T D_{ii}^{\text{rev}} \tag{24}$$

where, due to the incompressible character of the irreversible strains, D_{ii}^{rev} is equal to $\frac{\dot{J}}{J}$.

This last expression does not take into account the possible thermal dependencies of the elastic properties. To get the correct expression of the thermoelastic heating, we have to derive the constitutive equation

$$\boldsymbol{\sigma} = \mathscr{H} : \boldsymbol{\epsilon}^{\text{e}} \tag{25}$$

with respect to temperature, which results in

$$\frac{\partial \boldsymbol{\sigma}}{\partial T} = \frac{\partial \mathscr{H}}{\partial T} : \boldsymbol{\epsilon}^{\text{e}} + \mathscr{H} : \frac{\partial \boldsymbol{\epsilon}^{\text{e}}}{\partial T} = \left[\frac{\partial \mathscr{H}}{\partial T} : (\mathscr{H}^{-1} : \boldsymbol{\sigma}) \right] + \left[\mathscr{H} : \frac{\partial \boldsymbol{\epsilon}^{\text{e}}}{\partial T} \right] \tag{26}$$

where $\boldsymbol{\epsilon}^{\text{e}}$ is a representative tensor of the elastic deformation.

The first term in brackets can be written

$$\left[\frac{\partial \mathscr{H}}{\partial T} : (\mathscr{H}^{-1} : \boldsymbol{\sigma}) \right] = \frac{\partial G}{\partial T} \frac{\boldsymbol{s}}{G} + \frac{\partial K}{\partial T} \frac{p\boldsymbol{I}}{K} \tag{27}$$

and the second term in brackets (which is the classical term) is

$$-3K\beta\boldsymbol{I} \tag{28}$$

Thus the final general expression of the thermoelastic heating is

$$\dot{W}^{\text{thel}} = T\left(\frac{\partial G}{\partial T}\frac{\boldsymbol{s}}{G} + \frac{\partial K}{\partial T}\frac{p\boldsymbol{I}}{K} - 3K\beta\boldsymbol{I}\right) : \boldsymbol{D}^{\text{rev}} \tag{29}$$

or

$$\dot{W}^{\text{thel}} = T\left(\frac{\partial G}{\partial T}\frac{\boldsymbol{\sigma}}{G} + \left[\frac{\partial K}{\partial T}\frac{1}{K} - \frac{\partial G}{\partial T}\frac{1}{G}\right]p\boldsymbol{I} - 3K\beta\boldsymbol{I}\right) : \boldsymbol{D}^{\text{rev}} \tag{30}$$

Let us note that in that last equation, the term in brackets is null if only the Young's modulus depend on the temperature (which is usually the case for metals).

3. The enhanced assumed strain formalism

We now want to solve the equations which govern the mechanical part of the strongly coupled thermo-mechanical problem under consideration. These equations are given by

$$\rho\frac{\partial \boldsymbol{v}}{\partial t} = \rho\boldsymbol{b} + \operatorname{div}\boldsymbol{\sigma} \tag{31}$$

where the stress tensor $\boldsymbol{\sigma}$ results from the integration of the constitutive model (see Adam, 2003; Ponthot, 2002 for the integration procedure)

$$\overset{\triangledown}{\boldsymbol{\sigma}} = \mathscr{H}(T) : (\boldsymbol{D} - \boldsymbol{D}^{\text{p}} - \boldsymbol{D}^{\text{th}}) + \dot{\mathscr{H}}(T) : ((\mathscr{H}(T))^{-1} : \boldsymbol{\sigma}) \tag{32}$$

with

$$\boldsymbol{D} = \frac{1}{2}(\dot{\boldsymbol{F}}\boldsymbol{F}^{-1} + (\dot{\boldsymbol{F}}\boldsymbol{F}^{-1})^{\text{T}}) \tag{33}$$

given the initial conditions at $t = 0$

$$x = x|_{t=0} \quad v = v|_{t=0} \quad \boldsymbol{\sigma} = \boldsymbol{\sigma}|_{t=0} \quad \bar{\epsilon}^{\text{p}} = \bar{\epsilon}^{\text{p}}|_{t=0} \tag{34}$$

Usually, applying standard finite element procedure to Eq. (31) governing the motion of a body will result in a system of non-linear algebraic equations expressed as the assembly of the elementary internal and external forces vectors given by

$$\vec{F}^{\text{mec}}_{\text{int}} - \vec{F}^{\text{mec}}_{\text{ext}} = 0 \tag{35}$$

with

$$\vec{F}^{\text{mec}}_{\text{int}} = \mathscr{A}_{e=1}^{e=n}(\vec{F}^{\text{mec}}_{\boldsymbol{a}-e} + \vec{F}^{\text{mec}}_{\boldsymbol{\sigma}-e}) \tag{36}$$

$$\vec{F}^{\text{mec}}_{\text{ext}} = \mathscr{A}_{e=1}^{e=n}(\vec{F}^{\text{mec}}_{b-e}) \tag{37}$$

where $\mathscr{A}$ is the classical assembly operator, e is the element index, n the number of elements used to discretize the body, and where the elementary forces vector are given by

$$\vec{F}^{\text{mec}}_{\boldsymbol{a}-e} = \left(\int_{V^{\text{Iso}}} \rho\boldsymbol{\phi}\boldsymbol{\phi}^{\text{T}} J^{\text{Iso}}\,\mathrm{d}V^{\text{Iso}}\right)\boldsymbol{a} \tag{38}$$

$$\vec{F}^{\text{mec}}_{\boldsymbol{\sigma}-e} = \int_{V^{\text{Iso}}} \boldsymbol{B}\boldsymbol{\sigma} J^{\text{Iso}}\, \mathrm{d}V^{\text{Iso}} \tag{39}$$

$$\vec{F}^{\text{mec}}_{b-e} = \int_{V^{\text{Iso}}} \rho \boldsymbol{\phi}\boldsymbol{b} J^{\text{Iso}}\, \mathrm{d}V^{\text{Iso}} \tag{40}$$

where the integration domain is the element's isoparametric space, $\boldsymbol{\phi}$ is the matrix of the shape functions, J^{Iso} is the determinant of the Jacobian of the isoparametric transformation, a is the vector of nodal accelerations, and $\boldsymbol{B}$ is the matrix of the gradients of the shape functions. Notice that if forces resulting from imposed surface tractions or from contact interactions exist, they have to be collected in $\vec{F}^{\text{mec}}_{\text{ext}}$.

In an isothermal framework, when inertia forces $\vec{F}^{\text{mec}}_{\boldsymbol{a}}$ are negligible, solving these non-linear equations by a Newton scheme will give rise to successive linear systems which are written

$$\boldsymbol{K}^{\text{mec–mec}}_{T} \Delta \boldsymbol{z}^{\text{mec}} = \vec{F}^{\text{mec}}_{\text{ext}} - \vec{F}^{\text{mec}}_{\text{int}} \tag{41}$$

where $\boldsymbol{K}^{\text{mec–mec}}_{T}$ is the structural mechanical stiffness matrix and $\boldsymbol{z}^{\text{mec}}$ is the vector of mechanical unknowns (i.e. the displacements).

In the following, we will still use a conventional Galerkin finite element method to solve a weak form of Eq. (31). However, this weak form, results from the variation of a three fields variational principle of the Hu–Washizu type (Simo and Rifai, 1990; Simo and Armero, 1992; Simo et al., 1993) allowing the introduction of the enhancement of the deformation gradient.

The basic principle of the EAS formalism is thus to enrich the deformation gradient $\boldsymbol{F} = \frac{\partial \boldsymbol{x}}{\partial \boldsymbol{X}}$ of each element in order to enhance its accuracy. This enrichment consists in adding an enhanced deformation gradient $\boldsymbol{F}^{\text{enh}}$ so that the deformation gradient effectively used in the stress computations $\boldsymbol{F}^{\text{tot}}$ is

$$\boldsymbol{F}^{\text{tot}} = \boldsymbol{F} + \boldsymbol{F}^{\text{enh}} = \frac{\partial \boldsymbol{x}}{\partial \boldsymbol{X}} + \boldsymbol{F}^{\text{enh}} \tag{42}$$

That enhancement is done in order to add some modes of deformation that lack in $\boldsymbol{F}$ when using first order elementary shape functions (Andelfinger and Ramm, 1993). As stated before, the EAS formalism will enable us to have an almost locking-free response (depending on the number of additional modes of deformation-see Andelfinger and Ramm (1993)) with weak mesh instabilities.

Briefly (see Simo and Rifai, 1990; Simo and Armero, 1992; Simo et al., 1993 fore more details), to build an objective formulation, the enhanced part of the deformation gradient can be written as

$$\boldsymbol{F}^{\text{enh}} = \boldsymbol{F}_{\text{cen}} \boldsymbol{F}^{\text{eas}} \tag{43}$$

where $\boldsymbol{F}_{\text{cen}}$ is equal to the "material" deformation gradient at the element's center i.e. $\boldsymbol{F}_{\text{cen}} = \boldsymbol{F}|_{\boldsymbol{\xi}=0}$ where $\boldsymbol{\xi}$ are the coordinates in the element's isoparametric space.

The tensor $\boldsymbol{F}^{\text{eas}}$ is then defined in the reference configuration by transforming a pre-defined tensor $\boldsymbol{F}^{\text{modes}}$ described in the element's isoparametric space. That transformation is given by, following Simo et al. (1993):

$$\boldsymbol{F}^{\text{eas}} = \left(\frac{\det \boldsymbol{J}_{0\text{–cen}}}{\det \boldsymbol{J}_{0}}\right) \boldsymbol{J}_{0\text{–cen}} \boldsymbol{F}^{\text{modes}} \boldsymbol{J}^{-1}_{0\text{–cen}} \tag{44}$$

where $\boldsymbol{J}_0 = \frac{\partial \boldsymbol{X}}{\partial \boldsymbol{\xi}}$ and $\boldsymbol{J}_{0\text{–cen}} = \frac{\partial \boldsymbol{X}}{\partial \boldsymbol{\xi}}|_{\boldsymbol{\xi}=0}$.

An alternative transformation was also suggested by Glaser and Armero (1997) which increases, according to these authors, the quality of the results for elements with highly distorted geometry in the reference configuration. In the present case, where our formulation is based on an Updated Lagrangian approach, we have not observed, and thus not considered, such a modification.

Now we have to define the exact expressions of the deformation modes that we want to add to the elements i.e. the tensor $\boldsymbol{F}^{\text{modes}}$. This can be done using the following way:

$$\boldsymbol{F}^{\text{modes}} = \sum_{I=1}^{n\text{mod}} \boldsymbol{F}^{\text{mode}_I} \alpha^{\text{mod}_I} \tag{45}$$

Each of the $n$mod enhanced modes is further defined by a tensor $\boldsymbol{F}^{\text{mode}_I}$, and its amplitude is controlled by the unknown parameter α^{mod_I}. We send the interest reader back to the references (Simo and Rifai, 1990; Simo and Armero, 1992; Simo et al., 1993) to see restrictions that must be satisfied during the construction of the tensors $\boldsymbol{F}^{\text{mode}_I}$.

As we will use the EAS formalism in an incremental Updated Lagrangian framework, the modes α^{mod_I} will furnish at each time step a measure of the activation of the modes $\boldsymbol{F}^{\text{mode}_I}$ during the current step.

The weak form of the governing equations of the modes α^{mod_I} results from the second variation of the three fields variational principle (see Simo and Rifai, 1990; Simo and Armero, 1992; Simo et al., 1993), and from the use of the assumption that

$$\int_{V^{\text{Iso}}} \boldsymbol{F}^{\text{eas}} J^{\text{Iso}} \, \mathrm{d}V^{\text{Iso}} = 0 \tag{46}$$

which enables us to obtain a formulation which satisfies the patch test as demonstrated in (Simo and Rifai, 1990; Simo and Armero, 1992; Simo et al., 1993).

Thus, the algebraic equation governing the EAS mode α^{mod_I}, in element e, resulting from the second variation of the variational principle is given by

$$F^{\text{mec}}_{\alpha^{\text{mod}_I} - e} = \int_{V^{\text{Iso}}} \boldsymbol{G}^I : \boldsymbol{\sigma} J^{\text{Iso}} \, \mathrm{d}V^{\text{Iso}} = 0 \tag{47}$$

where

$$\boldsymbol{G}^I = \boldsymbol{F}_{\text{cen}} \boldsymbol{F}^{\text{eas}_I} (\boldsymbol{F}^{\text{tot}})^{-1} \tag{48}$$

and

$$\boldsymbol{F}^{\text{eas}_I} = \left(\frac{\det \boldsymbol{J}_{0\text{–cen}}}{\det \boldsymbol{J}_0} \right) \boldsymbol{J}_{0\text{–cen}} \boldsymbol{F}^{\text{mode}_I} \boldsymbol{J}^{-1}_{0\text{–cen}} \tag{49}$$

Equations such as (47) have to be assemble over all the elements and EAS modes, giving rise to the algebraic system of equations

$$\vec{F}^{\text{mec}}_{\alpha^{\text{mod}}} = \mathop{\mathscr{A}}_{e=1}^{e=n} \left[\mathop{\mathscr{A}}_{I=1}^{I=n\text{mod}} \left(\vec{F}^{\text{mec}}_{\alpha^{\text{mod}_I} - e} \right) \right] = 0 \tag{50}$$

In the classical expression of the internal elementary mechanical forces of the element $\boldsymbol{F}^{\text{mec}}_{\boldsymbol{\sigma}-e}$ the shape function gradients must be replaced by their EAS equivalent, which leads to

$$\vec{F}^{\text{mec}}_{\boldsymbol{\sigma}-e} = \int_{V^{\text{Iso}}} \boldsymbol{B}^{\text{tot}} \boldsymbol{\sigma} J^{\text{Iso}} \, \mathrm{d}V^{\text{Iso}} \tag{51}$$

where

$$\boldsymbol{B}^{\text{tot}} = (\boldsymbol{F}^{\text{tot}})^{-\text{T}} \left((\boldsymbol{J}_0)^{-\text{T}} \frac{\partial \boldsymbol{\phi}}{\partial \boldsymbol{\xi}} + (\boldsymbol{F}^{\text{eas}})^{\text{T}} \left((\boldsymbol{J}_{0-\text{cen}})^{-\text{T}} \frac{\partial \boldsymbol{\phi}}{\partial \boldsymbol{\xi}} \bigg|_{\xi=0} \right) \right) \tag{52}$$

which reduces to the classical expression when $\boldsymbol{F}^{\text{eas}} = 0$ i.e. when there is no enhanced assumed strain.

It is important to note that the resulting first order EAS element is no longer exactly integrated when using two Gauss integration points by spatial direction (see Simo et al., 1993 for details) and thus some

hourglassing modes could be activated. However, in this Updated Enhanced Lagrangian framework, hourglassing hardly appears when keeping a classical, first order, integration rule. Thus in the present formulation there is no major need to use higher order spatial integration rules or stabilization techniques.

Finally, the new linear system to solve at the structural level, resulting from the linearization of Eqs. (35) and (50), is given by

$$\begin{pmatrix} \boldsymbol{K}_T^{\text{mec–mec}} & \boldsymbol{K}_T^{\text{mec–eas}} \\ \boldsymbol{K}_T^{\text{eas–mec}} & \boldsymbol{K}_T^{\text{eas–eas}} \end{pmatrix} \begin{pmatrix} \Delta \boldsymbol{z}^{\text{mec}} \\ \Delta \boldsymbol{\alpha}^{\text{mod}} \end{pmatrix} = \begin{pmatrix} \vec{F}_{\text{ext}}^{\text{mec}} - \boldsymbol{F}_{\text{int}}^{\text{mec}} \\ \vec{F}_{\alpha^{\text{mod}}}^{\text{mec}} \end{pmatrix} \tag{53}$$

Instead of solving a fully coupled system which could lead to a much higher CPU time, this linear system is solved by static condensation of the equations governing the EAS modes over the equilibrium equations. The $n$mod equations $\vec{F}_{\alpha^{\text{mod}}}^{\text{mec}} = 0$ (cf. Eq. (47)) are solved at the element level by a classical or modified Newton scheme. The scalar components of the iteration matrix, used during this local resolution of the EAS modes, coupling the modes I and J are written

$$K_T^{\text{eas}_I-\text{eas}_J} = \int_{V^{\text{Iso}}} \boldsymbol{G}_{ij}^I \mathscr{L}_{ijkl} \boldsymbol{G}_{kl}^J J^{\text{Iso}} \, \mathrm{d}V^{\text{Iso}} \tag{54}$$

where $\mathscr{L}$ is the consistent tangent stiffness matrix of the mechanical equilibrium problem (see Ponthot, 2002; Adam, 2003).

As usual, it is of prime interest to compute an initial guess to start the local Newton scheme. This EAS modes guess is based on the rate of change of the modes during the last converged time step and on the ratio of the duration of the last and current step. Doing so, it is possible to solve the local problem in more or less 3 local iterations (in most case) with a modified Newton scheme (which involves only an initial computation of the iteration matrix).

The coupling elementary matrices between the mechanical degrees of freedom and the EAS modes, which are assemble to form $\boldsymbol{K}_T^{\text{mec–eas}}$ and $\boldsymbol{K}_T^{\text{eas–mec}}$, are written

$$K_{T-e}^{\text{node}_I-\text{eas}_J} = \int_{V^{\text{Iso}}} \boldsymbol{B}_{Ij}^{\text{tot}} \mathscr{L}_{ijkl} \boldsymbol{G}_{kl}^J J^{\text{Iso}} \, \mathrm{d}V^{\text{Iso}} \tag{55}$$

and

$$K_{T-e}^{\text{eas}_I-\text{node}_J} = \int_{V^{\text{Iso}}} \boldsymbol{G}_{ij}^I \mathscr{L}_{ijkl} \boldsymbol{B}_{Jl}^{\text{tot}} J^{\text{Iso}} \, \mathrm{d}V^{\text{Iso}} \tag{56}$$

The static condensation results in a modification of the mechanical elementary stiffness matrix used into an equation of type (41) given by

$$\boldsymbol{K}_{T-e}^{\text{mec–mec}} \text{ becomes } \boldsymbol{K}_{T-e}^{\text{mec–mec}} - \boldsymbol{K}_{T-e}^{\text{node–eas}} \left(\boldsymbol{K}_{T-e}^{\text{eas–eas}}\right)^{-1} \boldsymbol{K}_{T-e}^{\text{eas–node}} \tag{57}$$

Theoretically, a modification of the out-of-equilibrium forces vector is also required, and is given by

$$\vec{F}_{\text{ext}}^{\text{mec}} - \vec{F}_{\text{int}}^{\text{mec}} \text{ becomes } \vec{F}_{\text{ext}}^{\text{mec}} - \vec{F}_{\text{int}}^{\text{mec}} - \boldsymbol{K}_T^{\text{node}_I-\text{eas}_J} \left(\boldsymbol{K}_T^{\text{eas}_I-\text{eas}_J}\right)^{-1} \vec{F}_{\alpha^{\text{mod}}}^{\text{mec}} \tag{58}$$

However, due to the local solving scheme of the EAS modes (i.e. of the equations $\vec{F}_{\alpha^{\text{mod}}}^{\text{mec}} = 0$) this modification can be neglected without much altering the convergence process.

The local solving scheme of the EAS modes exposed here (which was also suggested in Simo et al. (1993)) is highly less memory consuming than traditional, purely structural, static condensation. It also enables to control, independently from the mechanical equilibrium resolution, the accuracy of the resolution of the EAS modes. Moreover, this local method is much simpler to implement in a Finite Element code as it almost limits the modifications required by the EAS formalism to the element level.

The EAS modes that we will use in the following (3D models) are:
The first three volumetric modes

$$\boldsymbol{F}_{\text{vol}}^{\text{mode}_1} = \begin{pmatrix} \xi & 0 & 0 \\ 0 & 0 & 0 \\ 0 & 0 & 0 \end{pmatrix} \quad \boldsymbol{F}_{\text{vol}}^{\text{mode}_2} = \begin{pmatrix} 0 & 0 & 0 \\ 0 & \eta & 0 \\ 0 & 0 & 0 \end{pmatrix} \quad \boldsymbol{F}_{\text{vol}}^{\text{mode}_3} = \begin{pmatrix} 0 & 0 & 0 \\ 0 & 0 & 0 \\ 0 & 0 & \rho \end{pmatrix} \tag{59}$$

which can be supplemented by the six volumetric modes

$$\boldsymbol{F}_{\text{vol}}^{\text{mode}_4} = \begin{pmatrix} \xi\eta & 0 & 0 \\ 0 & 0 & 0 \\ 0 & 0 & 0 \end{pmatrix} \quad \boldsymbol{F}_{\text{vol}}^{\text{mode}_5} = \begin{pmatrix} 0 & 0 & 0 \\ 0 & \eta\rho & 0 \\ 0 & 0 & 0 \end{pmatrix} \quad \boldsymbol{F}_{\text{vol}}^{\text{mode}_6} = \begin{pmatrix} 0 & 0 & 0 \\ 0 & 0 & 0 \\ 0 & 0 & \rho\xi \end{pmatrix} \tag{60}$$

$$\boldsymbol{F}_{\text{vol}}^{\text{mode}_7} = \begin{pmatrix} \xi\rho & 0 & 0 \\ 0 & 0 & 0 \\ 0 & 0 & 0 \end{pmatrix} \quad \boldsymbol{F}_{\text{vol}}^{\text{mode}_8} = \begin{pmatrix} 0 & 0 & 0 \\ 0 & \eta\xi & 0 \\ 0 & 0 & 0 \end{pmatrix} \quad \boldsymbol{F}_{\text{vol}}^{\text{mode}_9} = \begin{pmatrix} 0 & 0 & 0 \\ 0 & 0 & 0 \\ 0 & 0 & \rho\eta \end{pmatrix} \tag{61}$$

Regarding the shear modes, the six first are

$$\boldsymbol{F}_{\text{cis}}^{\text{mode}_1} = \begin{pmatrix} 0 & 0 & 0 \\ \xi & 0 & 0 \\ 0 & 0 & 0 \end{pmatrix} \quad \boldsymbol{F}_{\text{cis}}^{\text{mode}_2} = \begin{pmatrix} 0 & 0 & 0 \\ 0 & 0 & 0 \\ \xi & 0 & 0 \end{pmatrix} \quad \boldsymbol{F}_{\text{cis}}^{\text{mode}_3} = \begin{pmatrix} 0 & \eta & 0 \\ 0 & 0 & 0 \\ 0 & 0 & 0 \end{pmatrix} \tag{62}$$

$$\boldsymbol{F}_{\text{cis}}^{\text{mode}_4} = \begin{pmatrix} 0 & 0 & 0 \\ 0 & 0 & 0 \\ 0 & \eta & 0 \end{pmatrix} \quad \boldsymbol{F}_{\text{cis}}^{\text{mode}_5} = \begin{pmatrix} 0 & 0 & \rho \\ 0 & 0 & 0 \\ 0 & 0 & 0 \end{pmatrix} \quad \boldsymbol{F}_{\text{cis}}^{\text{mode}_6} = \begin{pmatrix} 0 & 0 & 0 \\ 0 & 0 & \rho \\ 0 & 0 & 0 \end{pmatrix} \tag{63}$$

Which can be supplemented by six other modes

$$\boldsymbol{F}_{\text{cis}}^{\text{mode}_7} = \begin{pmatrix} 0 & 0 & 0 \\ \xi\rho & 0 & 0 \\ 0 & 0 & 0 \end{pmatrix} \quad \boldsymbol{F}_{\text{cis}}^{\text{mode}_8} = \begin{pmatrix} 0 & 0 & 0 \\ 0 & 0 & 0 \\ \xi\eta & 0 & 0 \end{pmatrix} \quad \boldsymbol{F}_{\text{cis}}^{\text{mode}_9} = \begin{pmatrix} 0 & \eta\rho & 0 \\ 0 & 0 & 0 \\ 0 & 0 & 0 \end{pmatrix} \tag{64}$$

$$\boldsymbol{F}_{\text{cis}}^{\text{mode}_{10}} = \begin{pmatrix} 0 & 0 & 0 \\ 0 & 0 & 0 \\ 0 & \eta\xi & 0 \end{pmatrix} \quad \boldsymbol{F}_{\text{cis}}^{\text{mode}_{11}} = \begin{pmatrix} 0 & 0 & \rho\eta \\ 0 & 0 & 0 \\ 0 & 0 & 0 \end{pmatrix} \quad \boldsymbol{F}_{\text{cis}}^{\text{mode}_{12}} = \begin{pmatrix} 0 & 0 & 0 \\ 0 & 0 & \rho\xi \\ 0 & 0 & 0 \end{pmatrix} \tag{65}$$

4. Linear and quadratric thermal elements and their coupling with linear mechanical elements

Classical linear thermal elements were first implemented (4 nodes quad in 2D and 8 nodes hexaedron in 3D), and strongly coupled, to linear mechanical elements. In such classical elements, the thermal and mechanical nodes match as well as the thermal and mechanical Gauss integration points. Thus there is not a real need to use a transfer or mapping method to exchange thermal and/or mechanical informations between integration points in order to compute the thermomechanical couplings appearing in Eqs. (11 and 12).

Let us note that there is a small exception for the SRI formalism, as the volumetric strain D_{ii} is needed to compute the thermoelastic structural heating (Eq. (24)) at the thermal Gauss integration points. As, in the

SRI formalism, the volumetric strain is constant over the element it is not computed at each thermal integration points but only at the centroid of the element. Thus a trivial mapping is used to transfer this quantity from the centroid to the thermal integration points. This exception does not exist when using the EAS formalism.

When using quadratic thermal elements (8 nodes quad in 2D or 20 nodes hexaedron in 3D), the situation is no more the same. These elements are integrated using three quadrature points by spatial direction, thus mechanical and thermal quantities are no more computed at the same Gauss points. Transfer between Gauss points is thus required and made by using the mechanical or thermal shape functions depending on the nature of the data.

5. Integration procedure

Next to the finite element method used to manage the spatial integration of the momentum and energy equation, we will mainly use an isothermal staggered scheme in order to manage the thermomechanical coupling (Simo and Miehe, 1992; Adam and Ponthot, 2002a). In contrast to monolithic schemes, which solve all the mechanical and thermal equations simultaneously, staggered schemes aim at solving mechanical and thermal equations sequentially in order to lower the CPU cost. The interest of using such staggered schemes in the fields of metal forming can be found in Simo and Miehe (1992), Adam and Ponthot (2002a,b) and Adam (2003).

In the sequel we will use an isothermal staggered scheme together with a generalized mid-point scheme to integrate the heat equation (Hogge, 1977; Hugues, 1977).

Concerning the integration over a time step $[t_n, t_{n+1}]$, of the finite strain kinematics and of the constitutive law, we will use the assumption of a constant rate of deformation, in the co-rotational space, equal to (see Ponthot, 2002)

$$\boldsymbol{D} = \frac{1}{2}\frac{\ln[\boldsymbol{F}(t_{n+1})^{\mathrm{T}}\boldsymbol{F}(t_{n+1})]}{\Delta t} \tag{66}$$

where $\Delta t = t_{n+1} - t_n$.

With this assumption, the problem dealt with, at the constitutive level, for each integration points, is to find the new values of the variables $(\boldsymbol{\sigma}_{n+1}, \bar{\epsilon}^{\mathrm{p}}_{n+1})$ at t_{n+1}. These are obtained by integration of the local constitutive equations with initial conditions given by $(\boldsymbol{\sigma}_n, \bar{\epsilon}^{\mathrm{p}}_n)$ at t_n. To integrate these equations in time, we will rely on the general methodology of elastic-predictor/plastic-corrector (return mapping algorithm), as synthesized by Simo and Hughes (1987). For more details on the integration of the constitutive laws, we send the reader back to the reference Ponthot (2002).

6. Applications

In this section, we will describe three applications involving thermomechanical coupling and finite strains. As we are mainly interested in thermomechanical coupling, we will focus the analysis on the mechanical part and put the inertial effects aside. We will also concentrate on the effects arising from the anisothermal framework. The first application, an academic one, is the radial expansion of a thermoplastic cylinder. This example will be used as a validation. The second application will study the thermo-elastoplastic buckling of a cylindrical tube, application also known as Laursen's cylinder (Laursen, 1992). Through that numerical example, involving important shear and bending strains, we will compare the behavior of the EAS and SRI formalism and will analyze, both at the element level and for the global structural response, the differences appearing in the results. The third application will study the thermomechanical behavior of a shock

absorber device (as initially described in Beltran and Goicolea (1989)). The aim of this example is to show the interest of using mixed order finite element to model accurately the high temperature gradients which can appear due to frictional heating.

In the following the thermoelastic material properties are assumed to be constants. It is obvious that this assumption is not correct if important temperature variations appear. However, as previoulsy exposed, the present formulation can model temperature dependent material properties and, thus, be used with appropriate thermal evolution laws for the thermoelastic properties.

6.1. Radial expansion of a thermoplastic cylinder

This first application, which aims to model the radial expansion of an infinite thermoplastic cylinder, will enable us to compare the results obtain with both finite element formalisms (i.e. SRI and EAS) using first or second order thermal elements with results already presented in the scientific literature. This problem was studied by numerous authors, among others let us cite Argyris and Doltsinis (1981) and Simo and Miehe (1992).

The geometry of the thick-wall infinite cylinder is showed in Fig. 1. In the initial configuration, the internal and external radii are respectively $R_i = 100$ mm and $R_e = 200$ mm. The mechanical boundary conditions consist in an imposed radial displacement of 130 mm at the inner surface of the cylinder. In the sequel the radial displacement will be applied in different time intervals. As the cylinder is infinitely long, it is not allowed to deform in the axial direction. The whole external surface of the cylinder is considered to be adiabatic.

The material parameters are collected in Table 1. We will here use a linear isotropic hardening, and an initial yield stress which soften as the temperature increases. This thermal softening is linear and is given by

$$\sigma_0^{\mathrm{v}}(T) = \sigma_0^{\mathrm{v}}(T_{\mathrm{ref}})(1 - \omega_{\sigma^{\mathrm{v}}}(T - T_{\mathrm{ref}})) \tag{67}$$

Thus the yield stress is given by

$$\sigma^{\mathrm{v}}(\bar{\epsilon}^{\mathrm{p}}, T) = [\sigma_0^{\mathrm{v}}(T_{\mathrm{ref}})(1 - \omega_{\sigma^{\mathrm{v}}}(T - T_{\mathrm{ref}}))] + g\bar{\epsilon}^{\mathrm{p}} \tag{68}$$

The mesh will be composed of 10 elements through the thickness of the cylinder with one element along the axial direction, and 10 elements in the hoop direction for tridimensional models. The reference, or default, mesh uses SRI finite element with first order thermal field. The time discretization is adapted automatically following the rate of convergence of the iterations of the solver. A generalized mid-point procedure will be used to integrate the heat equation in time, here using the fully implicit scheme.

Fig. 2 shows the evolution of the temperature at the inner surface of the cylinder, and the evolution of the internal pressure to apply to impose the radial the displacement. These results were obtained using and infinitely fast process (i.e. an adiabatic process) which does not allow thermal conduction effects to take

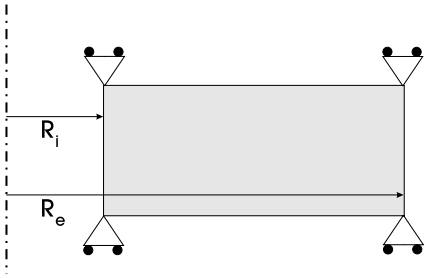

Fig. 1. Radial expansion of a thermoplastic cylinder: Geometry.

Table 1
Material properties of the cylinder

Young's modulus	$E = 70000$ MPa
Poisson's ratio	$\nu = 0.3$
Initial yield stress	$\sigma_0^{\mathrm{v}}(T_{\mathrm{ref}}) = 70$ MPa
Isotropic hardening modulus	$g = 210$ MPa
Thermal expansion coefficient	$\beta = 23.8 \times 10^{-6}\ \mathrm{K}^{-1}$
Conductivity	$k = 150$ W/(m K)
Initial density	$\rho_0 = 2700\ \mathrm{kg/m^3}$
Heat capacity	$c = 900$ J/(kg K)
Taylor–Quinney factor	$\chi = 0.9$
Thermal softening parameter of σ_0^{v}	$\omega_{\sigma^{\mathrm{v}}} = 3.0 \times 10^{-4}\ \mathrm{K}^{-1}$
Reference and initial temperature	$T_{\mathrm{ref}} = 293$ K

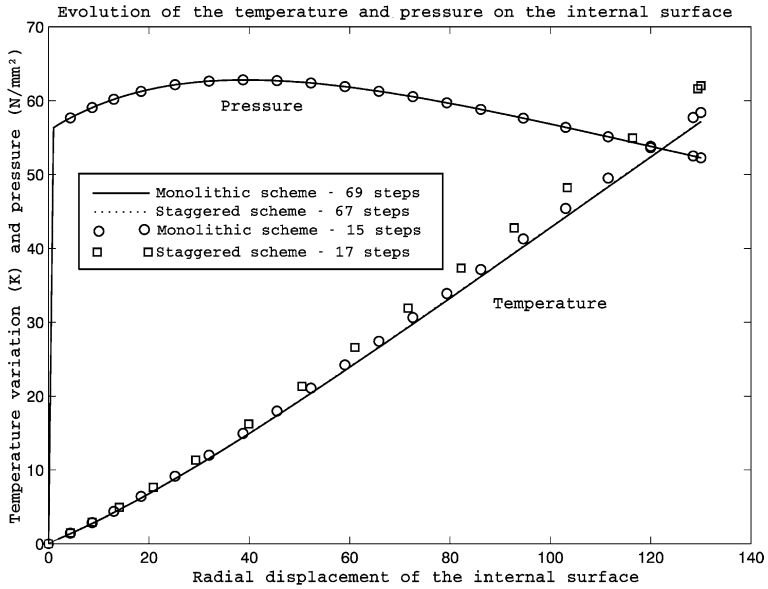

Fig. 2. Evolution of the temperature increase and pressure at the inner surface of the cylinder for different solution schemes and time discretizations—2D model.

place. We have here used both monolithic and isothermal staggered scheme with two different time discretizations.

Fig. 3 shows the evolution of the temperature field along the thickness of the cylinder for load cases which differ in their duration. The different loading duration are respectively $\rightarrow 0$ (adiabatic loading), 1.3, 13 and 130 s. We can notice the excellent matching of all theses results with those obtained by Simo and Miehe (1992).

Table 2 shows the upper and lower limits (located on the outer or inner surface of the cylinder) of the temperature and equivalent viscoplastic strain fields for the different finite element formalisms i.e. SRI and EAS with first and second order thermal elementary fields. The results were obtained using the isothermal staggered scheme and the adiabatic load case. We can thus note the good handling of the thermomechanical coupling between the linear mechanical fields and the quadratic thermal field both for the SRI and EAS formalisms.

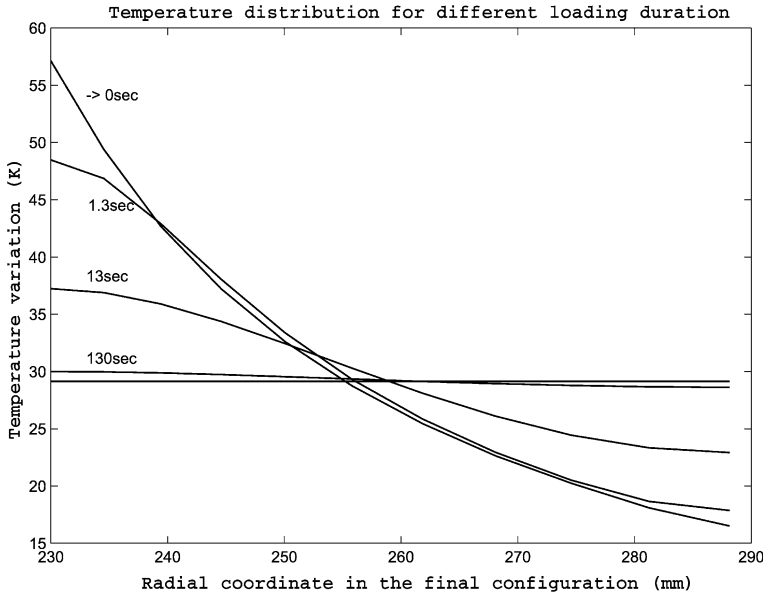

Fig. 3. Temperature increase fields for different loading durations—isothermal staggered scheme—2D model.

Table 2
Temperature and equivalent viscoplastic strain ranges for different finite element formalisms

Finite element formalism	$\Delta T^{\min}_{\text{outer}}$ (K)	$\Delta T^{\max}_{\text{inner}}$ (K)	$\bar{\epsilon}^{vp}_{\text{outer}}$	$\bar{\epsilon}^{vp}_{\text{inner}}$
2D SRI—linear temperature	16.5	57.0	0.426	0.932
2D SRI—quadratic temperature	17.4	58.9	0.426	0.935
3D SRI—linear temperature	16.5	57.1	0.426	0.933
3D SRI—quadratic temperature	17.4	58.9	0.426	0.936
3D EAS—linear temperature	17.0	58.3	0.418	0.954
3D EAS—quadratic temperature	17.6	59.7	0.418	0.957

6.2. Thermo-elastoplastic buckling of a cylindrical tube

This application models the thermomechanical buckling of a cylindrical tube during its crushing over a rigid foundation. Buckling phenomenon induces the creation of many folds in the cylinder and thus of important shear bending strains. This application was previously studied by Laursen (1992) in an isothermal context.

The setting is illustrated in Fig. 4. The geometry is axisymmetric but we will use a full three dimensional model to study this application. Thus we will study one quarter of the cylinder. The total cylinder top displacement Dz is imposed equal to 100 mm and is applied within 0.01 s. The temperature of the top of the cylinder is maintained at the initial temperature (i.e. 293 K). The other faces are considered adiabatic.

The constitutive behavior of the cylinder is thermo-elastoplastic with a thermal softening of the hardening properties (the constitutive properties are collected in Table 3). The thermal softening of the yield stress and hardening modulus are linear in the temperature variation and are introduced through the parameters ω_{σ^v} and ω_g. The anisothermal isotropic hardening law is thus written

$$\sigma^v(\bar{\epsilon}^p, T) = \sigma^v_0(T) + g(T)\bar{\epsilon}^p = [\sigma^v_0(T_{\text{ref}})(1 - \omega_{\sigma^v}(T - T_{\text{ref}}))] + [g(T_{\text{ref}})(1 - \omega_g(T - T_{\text{ref}}))]\bar{\epsilon}^p \tag{69}$$

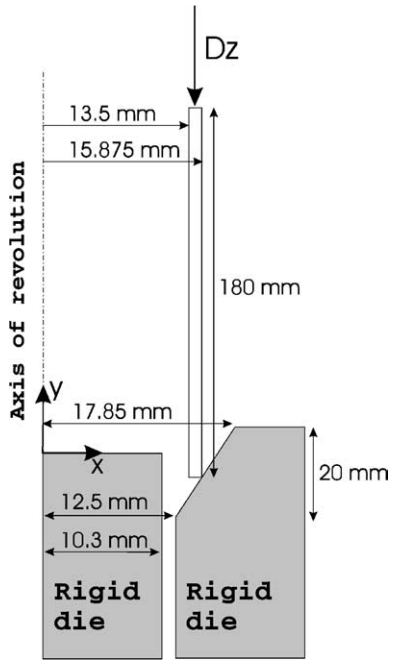

Fig. 4. Initial geometry (2D view).

Table 3
Material properties for the cylinder

Young's modulus	$E = 210000$ MPa
Poisson's ratio	$\nu = 0.3$
Yield stress at room temperature	$\sigma_0^{\mathrm{v}}(T_{\mathrm{ref}}) = 700$ MPa
Linear hardening modulus at room temperature	$g(T_{\mathrm{ref}}) = 808$ MPa
Thermal expansion coefficient	$\beta = 2.38 \times 10^{-5}\ \mathrm{K}^{-1}$
Conductivity	$k = 150$ W/(m K)
Initial density	$\rho_0 = 7850\ \mathrm{kg/m}^3$
Heat capacity	$c = 900$ J/(kg K)
Taylor–Quinney factor	$\chi = 0.9$
Thermal softening parameter of σ_0^{v}	$\omega_{\sigma^{\mathrm{v}}} = 2.0 \times 10^{-3}\ \mathrm{K}^{-1}$
Thermal softening parameter of g	$\omega_g = 2.0 \times 10^{-3}\ \mathrm{K}^{-1}$
Reference and initial temperature	$T_{\mathrm{ref}} = 293$ K

The contact interaction between the cylinder and the rigid dies is based on the Coulomb's law of friction (see Table 4 for the parameters). Concerning the contact interaction between the cylinder and itself (since folds are created) a frictionless behavior was supposed. In all cases it is important to notice that the sliding distances are negligible for the self-contact interaction and small for the interaction between the cylinder and the die. Thus, frictional heat dissipation will be here neglected due to its small contribution to the overall heating of the structure. The parameters relating to the self-contact interaction are collected in Table 5.

From the computational point of view contact constraints are imposed thanks to a penalty algorithm (see Laursen, 2002; Wriggers, 2002; Zhong, 1993 for more details). The penalty parameters are given in Tables 4 and 5.

Table 4
Parameters of the Coulomb's law of friction for the interaction between the cylinder and the moulds

Normal penalty coefficient	$c_N = 1.0 \times 10^6$ N/m
Tangential penalty coefficient	$c_T = 1.0 \times 10^5$ N/m
Coefficient of friction	$\mu = 0.2$

Table 5
Parameters of the frictionless self-contact interaction of the cylinder

Normal penalty coefficient	$c_N = 1.0 \times 10^7$ N/m

Fig. 5 shows different configurations of the cylinder during its crushing (on these figures half of the cylinder is actually represented). We clearly see the folds appearing due to the buckling mode of deformation, each center of these folds being the spot of an important plastic straining and thus of a temperature rise. Due to the thermal softening a localization effect appear at theses points which tends to decrease the capacity of the cylinder to sustain a load.

Figs. 6 and 7 show respectively the distribution of the equivalent plastic strain and the temperature field in the neighborhood of the first formed fold (time $t = 0.005$ s) when using the classical SRI formalism. Figs. 8 and 9 show the same distributions for the EAS formalism. On these figures, we can point out the good matching between the results given by the two finite element formalisms.

Fig. 10 shows a characteristic evolution of the force needed to apply the vertical displacement Dz (in other words the reaction force at the cylinder's top surface). We observe in this figure a quasi-cyclic evolution of the force due to the repeated creation of folds. A cycle is composed of a growing phase corresponding to the compression of the cylinder without creation of a new fold. Next, the force reaches a maximum which, globally, indicates the creation of a fold. Finally, the force decreases until the newly formed fold closes on itself (self-contact) leading to a similar configuration as the initial one, but with a shorter global length of the cylinder.

Due to the presence of a quasi-cyclic process of deformation we will study, in more details, only the first half of the process (final time $t = 0.005$ s) which gives rise to the forming and closing of at least one fold.

Let us now consider in more depth the differences existing between the structural response given by the SRI and EAS formalisms. The mesh that will be used for the comparisons is composed of 80 elements through the length of the cylinder and 6 elements along the polar direction. The number of elements through the thickness will be adjusted to assess the capacity of each formalism to accurately model large shear and bending strains (mesh dependency).

Fig. 11 shows the evolution of the crushing force, obtained for several discretizations, using SRI elements. Notice that the model fails before the end of the process when using a single layer of elements through the thickness. We also notice that 6 elements are needed to have a structural response that seems to be converged with respect to mesh dependency. The same evolutions, obtained with the EAS formalism, are drawn in Fig. 12. Nine EAS modes (six shear modes and three volumetric modes) have been used for theses results. We note that for the EAS elements, only 3 or 4 elements through the thickness are sufficient enough to deliver a converged result. We can also notice that the forming of the first fold is delayed when using the SRI formalism due to shear locking. This clearly appears in Fig. 13 which compares the "converged" response given by both formalisms.

Figs. 14 and 15 show, respectively for the SRI and EAS formalisms, the comparison of the crushing force resulting from an isothermal model and from an anisothermal model as previously studied. We can thus estimate the strength decrease of the cylinder due to the thermomechanical coupling and the temperature rise.

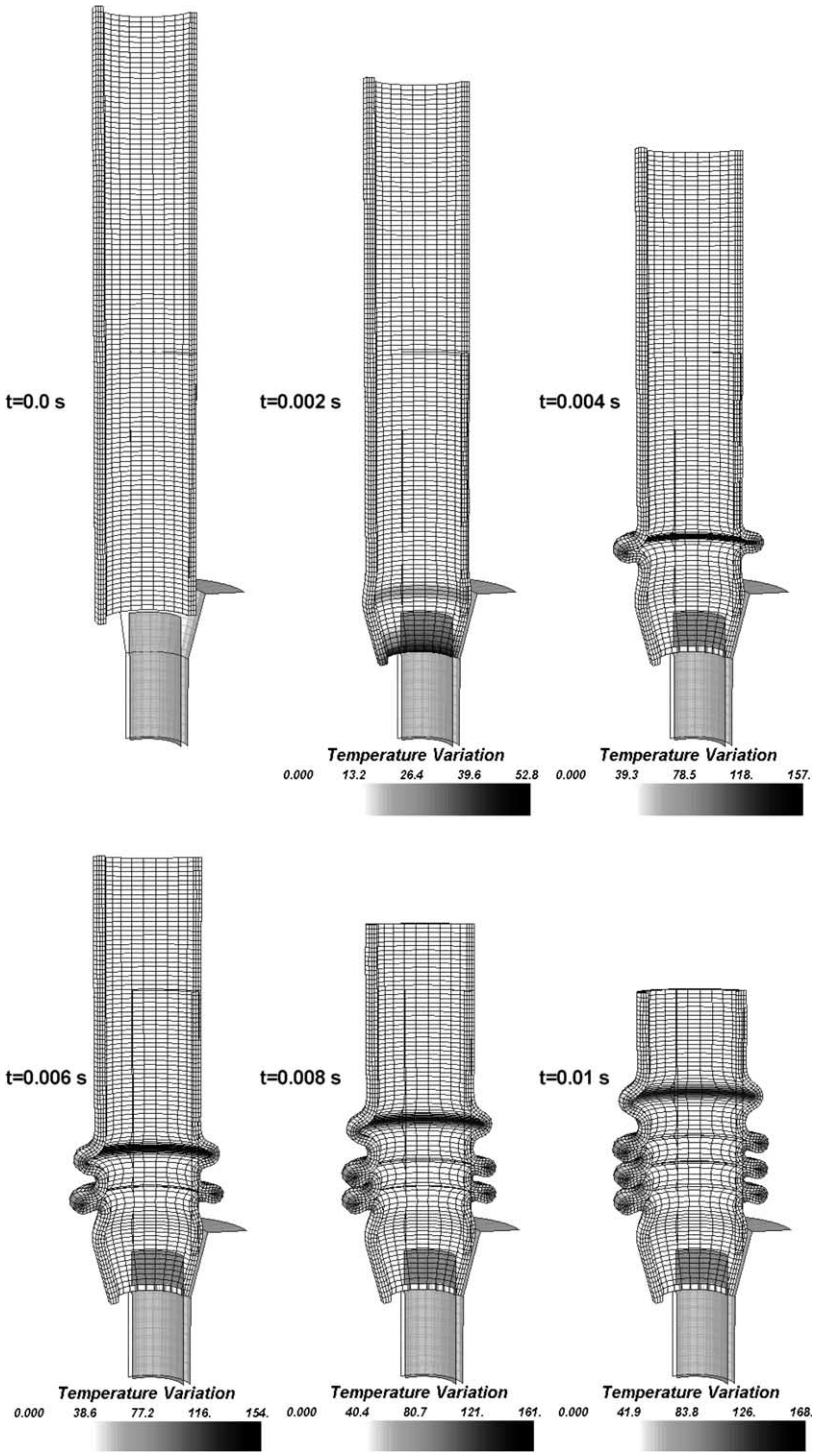

Fig. 5. Evolution of the configuration of the cylinder and temperature field—SRI formalism.

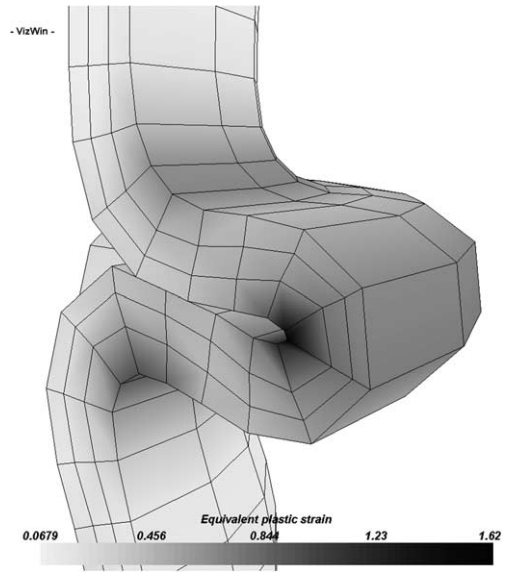

Fig. 6. Distribution of the equivalent plastic deformation in the neighborhood of the first formed fold (time $t = 5 \times 10^{-3}$ s)—SRI formalism.

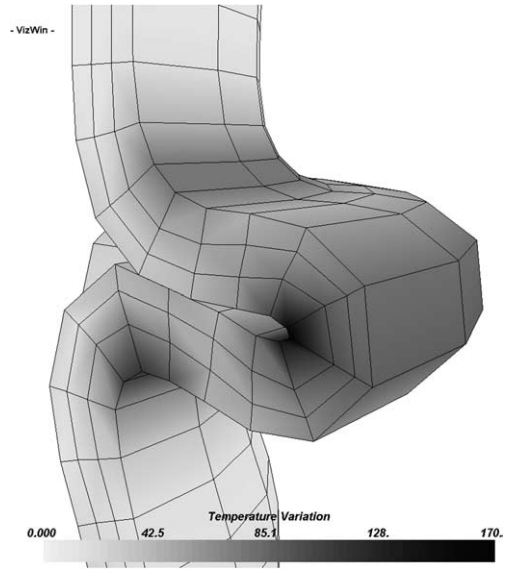

Fig. 7. Distribution of the temperature variation in the neighborhood of the first formed fold (time $t = 5 \times 10^{-3}$ s)—SRI formalism.

Finally, Fig. 16 proves that the variations observed in the results when increasing the number of EAS modes are negligible.

This application has showed that important differences can appear between the results given by the SRI and EAS formalisms when studying application involving important shear and bending strains. As exposed in Adam (2003), the CPU overcost induced by the EAS formalism becomes negligible for large models due

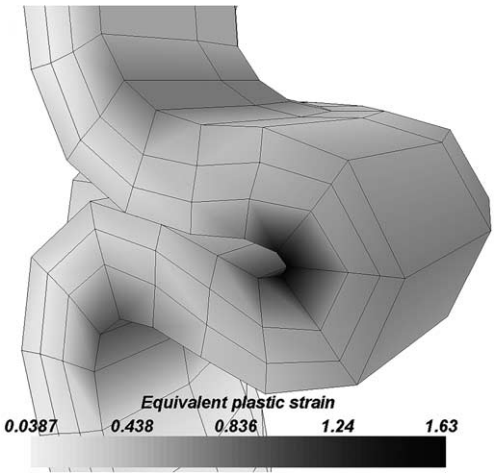

Fig. 8. Distribution of the equivalent plastic deformation in the neighborhood of the first formed fold (time $t = 5 \times 10^{-3}$ s)—EAS formalism.

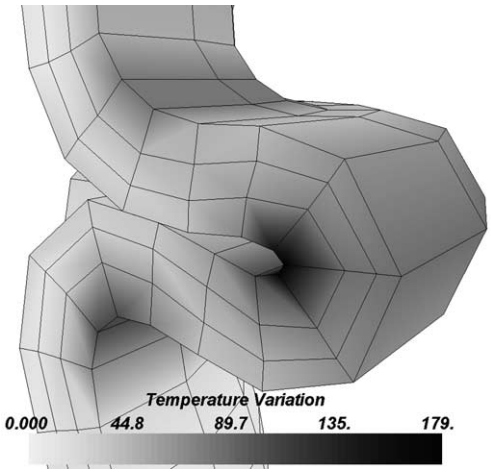

Fig. 9. Distribution of the temperature variation in the neighborhood of the first formed fold (time $t = 5 \times 10^{-3}$ s)—EAS formalism.

to the fact that the overcost is localized at the element's integration points and not at the structural level (the number of global unknowns being the same for both formalism). A characteristic evolution of the CPU cost, per iteration of the Newton, involved by both finite element formalisms is shown in Fig. 17.

6.3. Impact of a shock absorber device

This application aims at modeling the impact of a cylindrical structure over a rigid die. This kind of structure is used in the automotive industry to transform kinetic energy into plastic and thermal energy during crashes (shock absorber device). We will here study this application with two different impact speeds to show the interest to use mixed order element when temperature gradients become important. This problem has been previously studied by Beltran and Goicolea (1989) (quasi-static formulation), by Garcia Garino

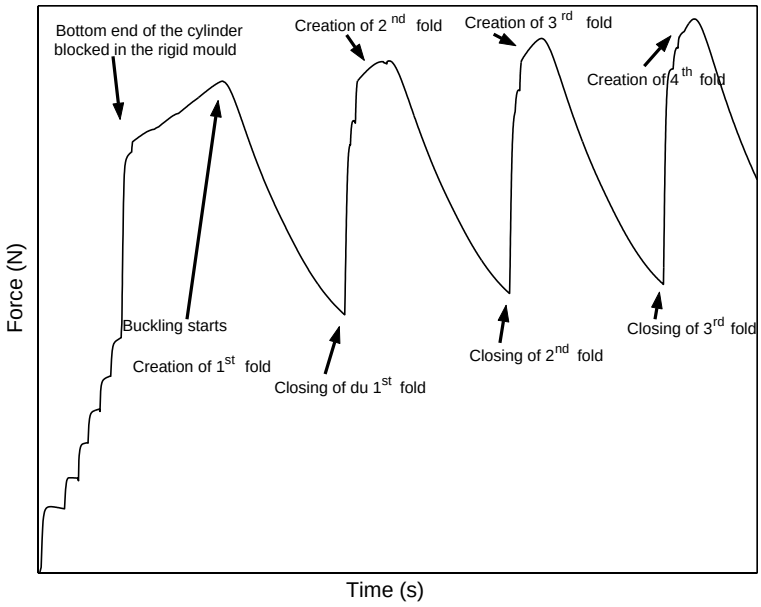

Fig. 10. Characteristic evolution of the force needed to crush the cylinder.

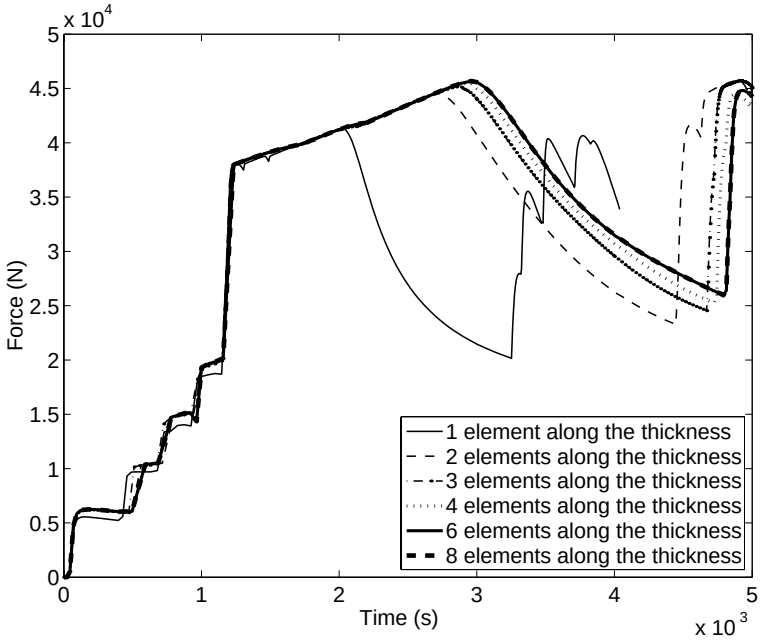

Fig. 11. Evolution of the crushing force—SRI formalism.

(1993) (explicit dynamic formulation) and by Ponthot (1995) (implicit dynamic formulation). All these authors have used isothermal bi-dimensional models. Thus the following study extends these results to the anisothermal behavior of the structure.

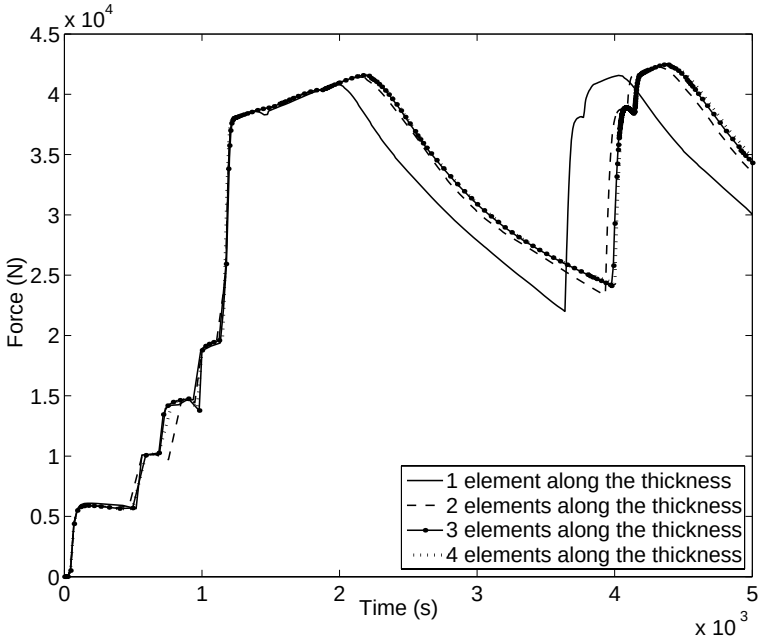

Fig. 12. Evolution of the crushing force—EAS formalism.

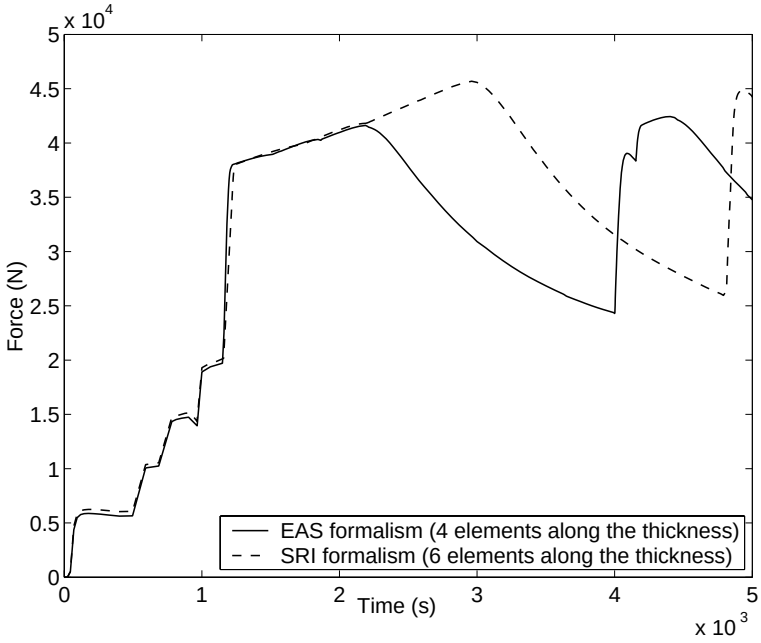

Fig. 13. Evolution of the crushing force—comparison between the SRI and EAS formalism.

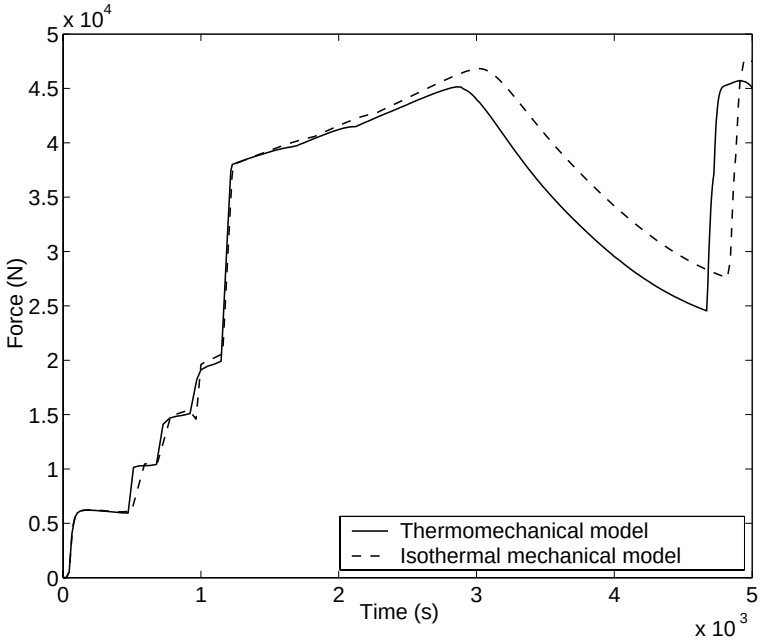

Fig. 14. Evolution of the crushing force—isothermal and anisothermal SRI formalism.

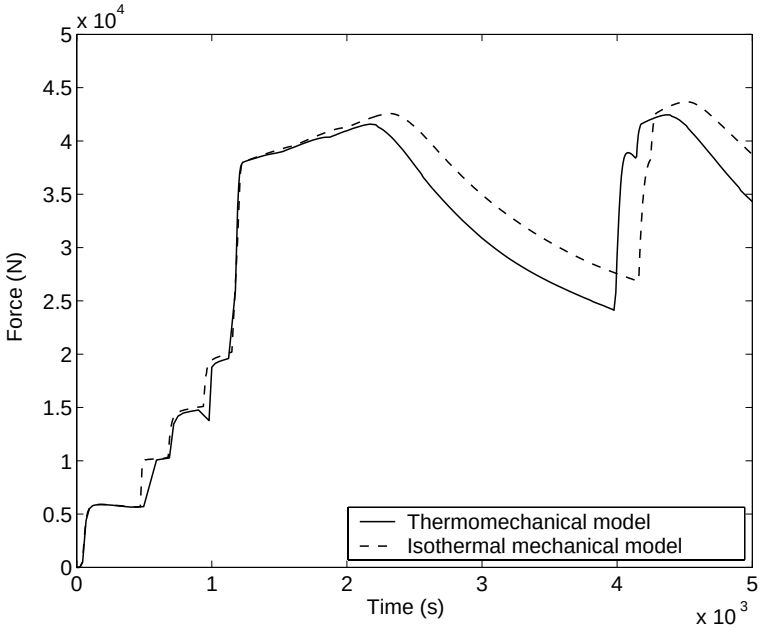

Fig. 15. Evolution of the crushing force—isothermal and anisothermal EAS formalism.

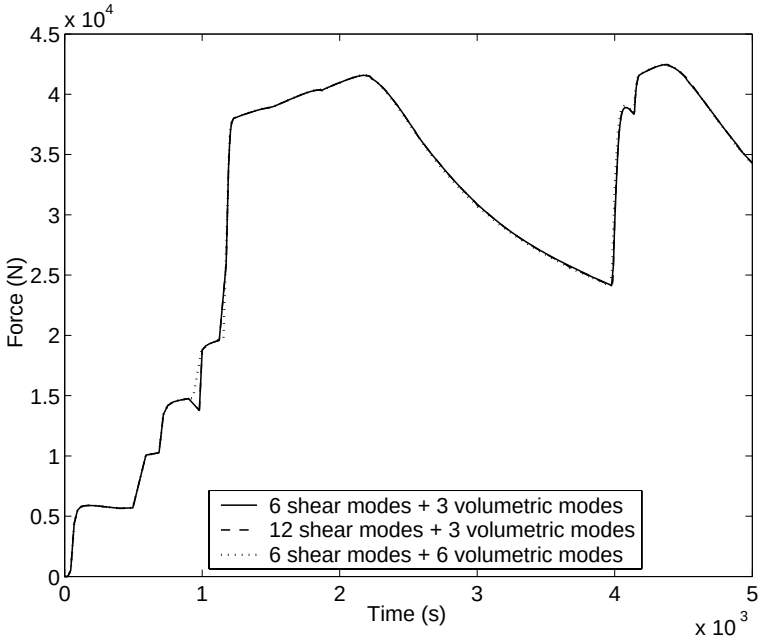

Fig. 16. Evolution of the crushing force—sensitivity of the solution with respect to the EAS enrichment.

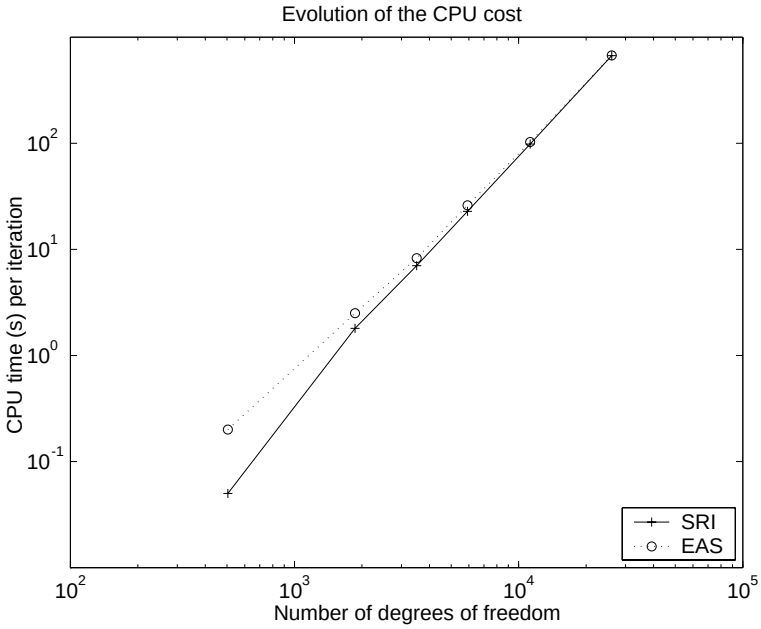

Fig. 17. Characteristic evolution of the CPU cost with the number of degrees of freedom involved by SRI and EAS formalisms.

The geometry of the tube is drawn in Fig. 18. In the following we will mainly build 2D models, since the structure is axisymmetric, but we will also show some results obtained while using 3D models.

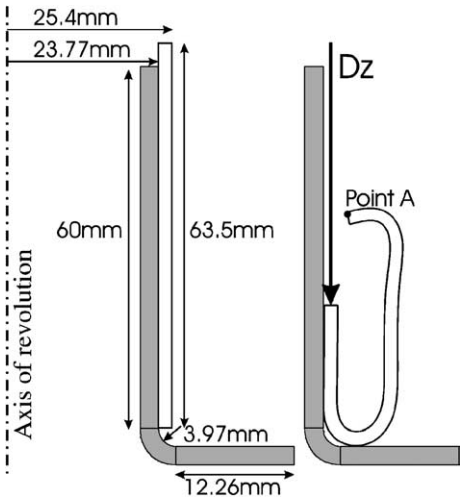

Fig. 18. Initial and deformed geometry (2D view).

Two impact speeds will be studied, respectively 1 km/h and 55 km/h. The impact is modeled through the application of a given vertical displacement of 50 mm at the top surface of the tube. Thus the impact will last respectively 0.18 s and 3.27×10^{-3} s. This imposed displacement is, with the thermocontact interaction between the tube and the mould, the only non-trivial boundary conditions used in the model.

The material behavior is of the thermo-elastoplastic type with linear isotropic hardening and linear thermal softening of the initial yield stress. The parameters charaterizing the current material behavior are collected in Table 6.

Concerning the thermocontact interactions, only the frictional heating will be computed. Heat exchanged between the tube and the die is quite smalls due to the short duration of the process. The parameters of the thermocontact interaction are collected in Table 7. We will also model a linear thermal softening of the coefficient of friction through the use of a parameter ω_μ.

The mesh used in this application consists of 6×100 SRI finite elements. The mesh is sufficiently refined to model accurately the deformation of the tube.

6.3.1. Crushing at 1 km/h

Figs. 19–23 show the temperature fields at five different times. We can point out that, due to the configuration of the tube and die, the frictional dissipation is the main heat source at the beginning of the process.

Table 6
Material properties of the cylinder

Young's modulus	$E = 67000$ N/mm^2
Poisson's ratio	$\nu = 0.3$
Yield stress	$\sigma_0^{\mathrm{v}}(T_{\mathrm{ref}}) = 150$ MPa
Linear hardening modulus	$g = 44.7$ MPa
Density	$\rho = 2.7 \times 10^{-9}$ N s^2/mm^4
Thermal expansion coefficient	$\beta = 23.86 \times 10^{-6}$ K^{-1}
Conductivity	$k = 150$ N/s K
Heat capacity	$c = 0.9 \times 10^9$ mm^2/s^2 K
Taylor–Quinney factor	$\chi = 0.9$
Linear thermal softening parameter of σ_0^{v}	$\omega_{\sigma^{\mathrm{v}}} = 2.0 \times 10^{-3}$ K^{-1}
Reference and initial temperature	$T_{\mathrm{ref}} = 293$ K

Table 7
Thermocontact parameters

Normal penalty coefficient	$c_N = 10^5$ N/mm
Tangential penalty coefficient	$c_T = 10^4$ N/mm
Coefficient of friction at 1 km/h	$\mu = 0.15$
Coefficient of friction at 55 km/h	$\mu = 0.08$
Relative effusivity	$\eta = 0.5$
Linear thermal softening parameter of the coefficient of friction	$\omega_\mu = 2.0 \times 10^{-3}$ K^{-1}

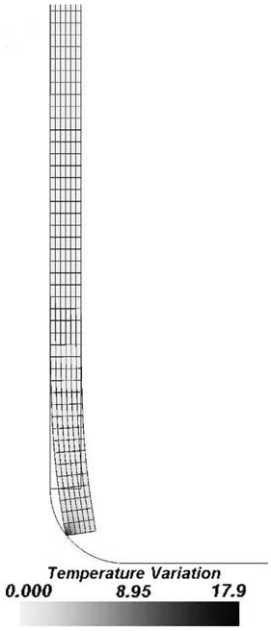

Fig. 19. Temperature fields—crushing at 1 km/h. Time: 0.009 s.

The frictional heating thus induces a temperature rise at the inner surface of the bottom end of the tube. This rise mainly affects the frictional coefficient which tends to decrease. At time $t = 0.036$ s (20% of the process duration) bulk plastic heating becomes more important because the tube turns inside out which creates a large zone of huge strain which growth as the process evolves. This plastic heating mainly affects the behavior of the continuum due to the softening of the yield stress.

The isotherms of the final temperature field are drawn in Fig. 24. We can clearly note the curvature of the isotherms which indicates the temperature rise due to the frictional heating.

The evolution of the vertical force, per unit hoop angle, needed to crush the tube is represented in Fig. 25. We have also drawn on this figure various evolutions obtained when setting the coefficient of friction to a null value, when keeping this coefficient to a constant value (no thermal softening), when suppressing all the thermal softening effects and when modeling an isothermal process. We thus conclude that, in this case, thermal softening induces a decrease of around 5% of the final value of the crushing force, and that this decrease is mainly due to the softening of the yield stress. We can also notice that a more important decrease in the coefficient of friction could have led to an important decrease of the crushing force.

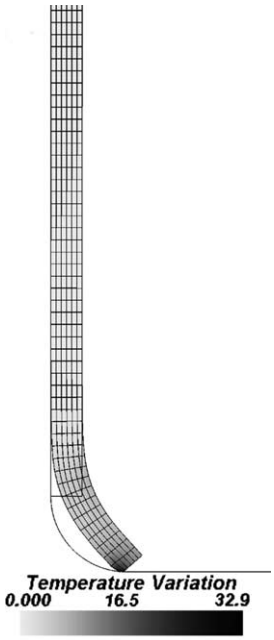

Fig. 20. Temperature fields—crushing at 1 km/h. Time: 0.018 s

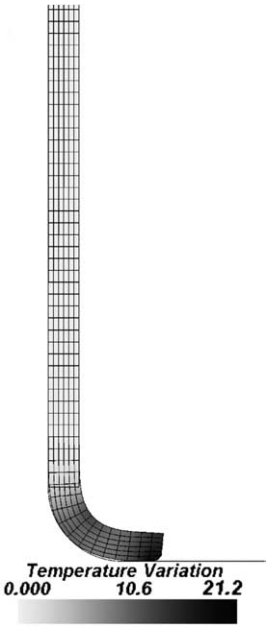

Fig. 21. Temperature fields—crushing at 1 km/h. Time: 0.027 s.

In Fig. 25 we can remark that tiny temporal oscillations appear in the evolution of the crushing force. These oscillations are also present, and more important, in the results of Beltran and Goicolea (1989) and

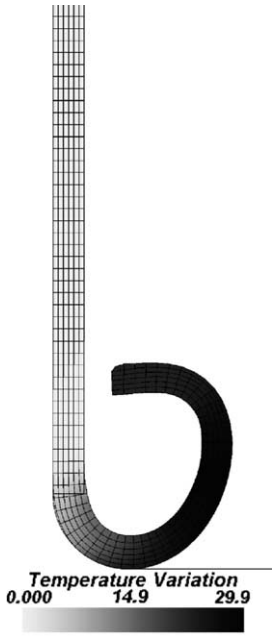

Fig. 22. Temperature fields—crushing at 1 km/h. Time: 0.09 s.

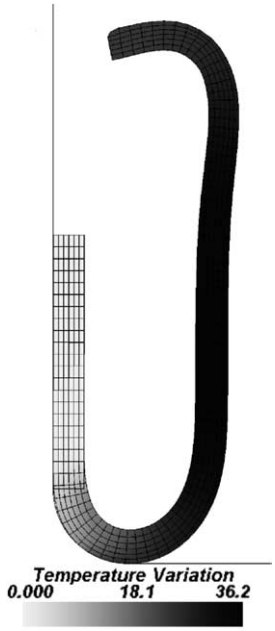

Fig. 23. Temperature fields—crushing at 1 km/h. Time: 0.18 s.

are due, according to these authors, to the use a the penalty method to manage contact. Fig. 26 illustrates their results, for a null coefficient of friction, obtained with the explicit code PR2D and the implicit code

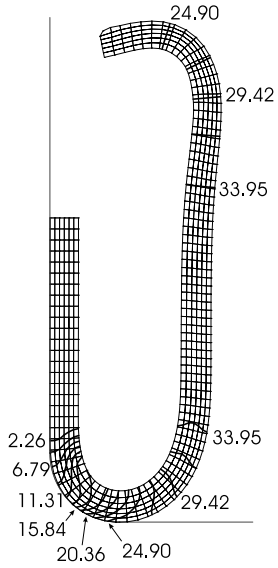

Fig. 24. Isotherms of the final temperature field (K) representing the increase with respect to room temperature—crushing at 1 km/h.

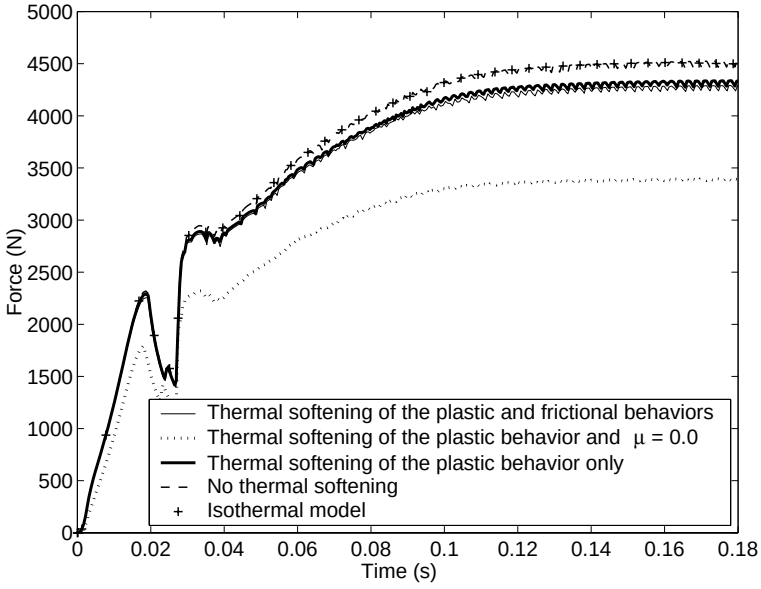

Fig. 25. Evolution of the crushing force (per unit hoop angle)—crushing at 1 km/h.

NIKE2D (note that the evolution obtained with the explicit code has been smoothed in order to filter higher frequencies). Their remark is only partially true since, following our experience, the use of a more strict mechanical equilibrium definition, i.e. the tolerance under which equilibrium is accepted, tends to decrease these oscillations back to satisfactory level.

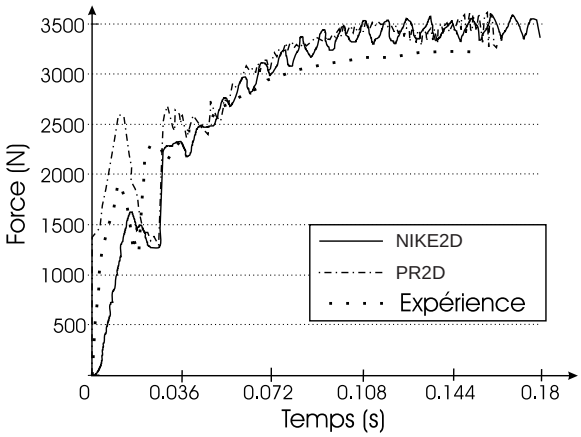

Fig. 26. Evolution of the crushing force (per unit hoop angle)—results obtained by Beltran and Goicolea (1989) for a frictionless contact interaction.

Fig. 27 shows the evolution of the temperature at point A (see Fig. 18) when using first order and second order thermal elements (the total number of elements being the same). We can confirm that the frictional dissipation mainly affects the thermal field at point A during the beginning of the process, and that the final temperature is more or less the same when neglecting or not the frictional interaction since, from a global point of view, it is driven by the plastic dissipation. We can also notice that the peak appearing in the temperature evolution is a little bit less pronounced when using the mixed order elements. As explained in details Adam (2003), this is due to the frictional heat flux distribution used in the mixed order thermocontact elements. This distribution tends to spread the heat flux over the main contact node (which is an edge

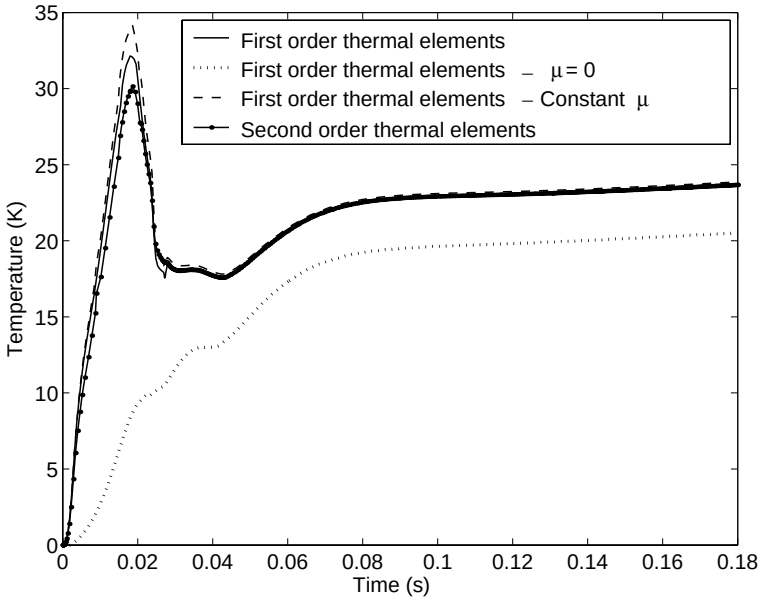

Fig. 27. Evolution of the temperature at point A—crushing at 1 km/h.

node) and its interfaces nodes, whereas the first order thermocontact element applied the flux on the single contact node. The spreading of the fluxes thus induces a less localized temperature increase.

In conclusion we can point out that at this crushing rate, the use of mixed order element is not essential since the mechanical and thermal behavior of the tube seems to be well computed by classical first order elements.

Similar results can be obtained using tridimensional models. For example, Figs. 28–30 show three temperature fields for 3D models based on SRI elements ($6 \times 100 \times 10$ elements). The same distributions obtained with the EAS formalism (here with the classical 6+3 enhanced modes) are shown in Figs. 31–33. We can thus point out only small differences in the results when using the SRI or EAS formalism. Fig. 34 shows the crushing force obtained with the two formalisms. We can point out the matching between both results but also the more important oscillatory behavior than for 2D models (this is an effect due to the discretization in the hoop direction). Note that the CPU cost involved by the use of higher penalty coefficients, or the use of a more strict equilibrium tolerance, to decrease the amplitude of the oscillations is quite important.

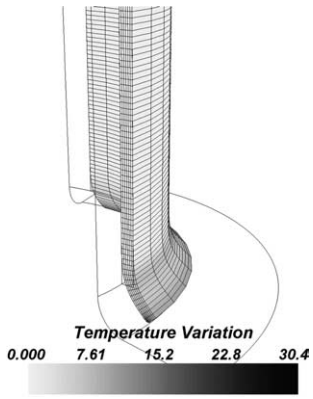

Fig. 28. Temperature field—3D model—SRI formalism—crushing at 1 km/h. Time: 0.018 s.

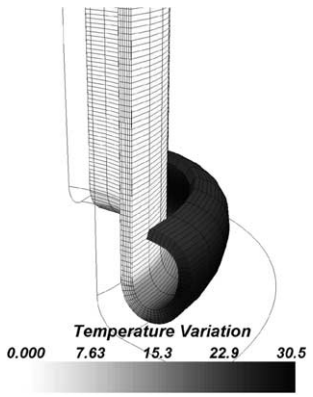

Fig. 29. Temperature field—3D model—SRI formalism—crushing at 1 km/h. Time: 0.09 s.

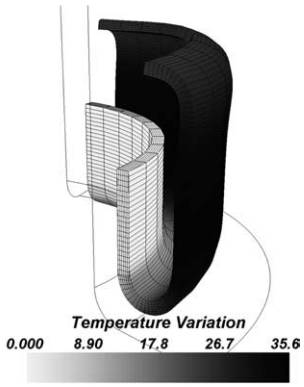

Fig. 30. Temperature field—3D model—SRI formalism—crushing at 1 km/h. Time: 0.18 s.

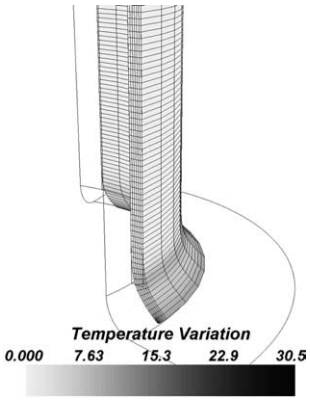

Fig. 31. Temperature field—3D model—EAS formalism—crushing at 1 km/h. Time: 0.018 s.

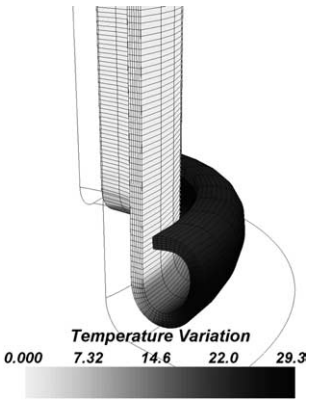

Fig. 32. Temperature field—3D model—EAS formalism—crushing at 1 km/h. Time: 0.09 s.

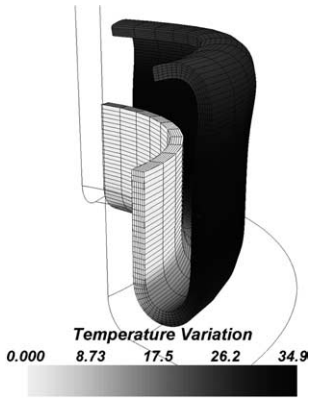

Fig. 33. Temperature field—3D model—EAS formalism—crushing at 1 km/h. Time: 0.18 s.

6.3.2. Crushing at 55 km/h

In the following we will continue to use the same finite element discretization as in the previous section. This choice is fully justified from a mechanical point of view, since we here suppose the constitutive behavior to be thermo-elastoplastic i.e. rate independent.

Figs. 35–38 show four temperature distributions at different times for the current crushing speed. We can thus point out that, due to the increase in crushing speed, oscillations appear in the temperature field (this effect is also known as 'skin effect'). Indeed, the temperature gradients to be modeled close to the inner skin of the tube have a characteristic length which is smaller than the characteristic element size, which leads to oscillations in the temperature field. Theses oscilations are mainly observed during the first phase of the process, and in the neighborhood of point A, due to the high frictional dissipation. Notice that in Fig. 35 these oscillations lead to negative temperatures which are not physical.

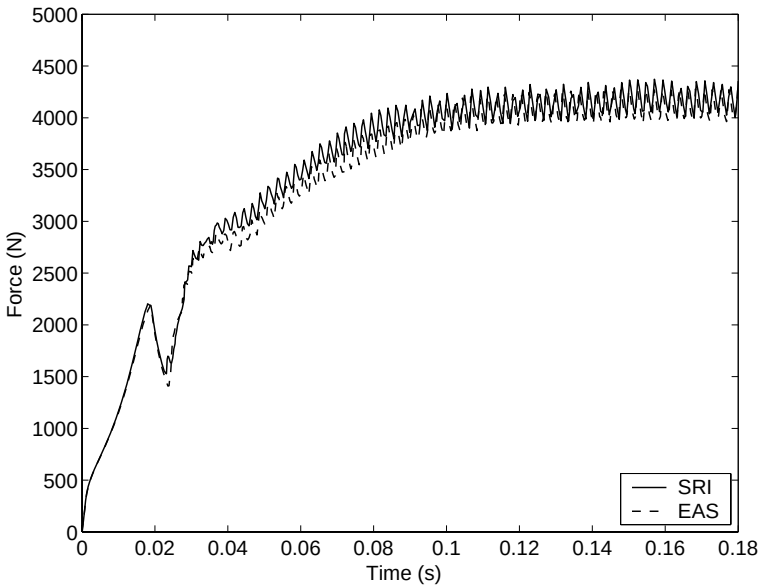

Fig. 34. Evolution of the crushing force (per unit angle)—3D model—crushing at 1 km/h—EAS and SRI formalisms.

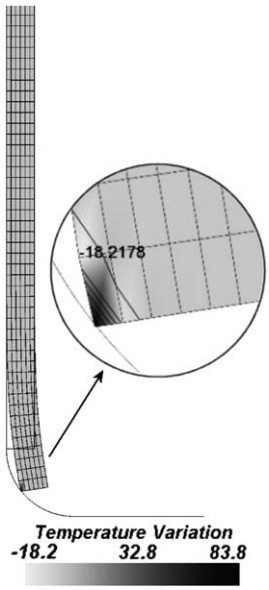

Fig. 35. Temperature fields—first order element—crushing at 55 km/h. Time: 1.636×10^{-4} s.

In the present case, the use of mixed order finite elements will enable us to model adequately the thermal behavior (i.e. to kill out the oscillations) without increasing the number of mechanical unknowns as it would happen with a classical mesh refinement. The temperature field obtained with these mixed elements are shown in Figs. 39–42 (on these figures the diamond patterns, which link the thermal interface nodes, superimposed to each element is just there to show that mixed order elements have been used). We can thus

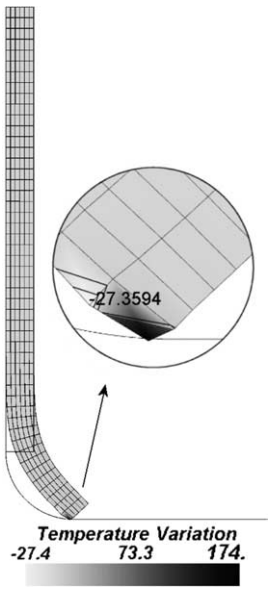

Fig. 36. Temperature fields—first order element—crushing at 55 km/h. Time: 3.273×10^{-4} s.

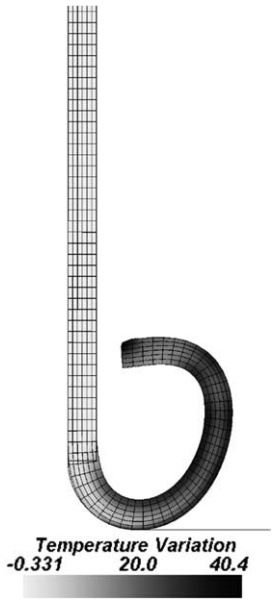

Fig. 37. Temperature fields—first order element—crushing at 55 km/h. Time: 1.636×10^{-3} s.

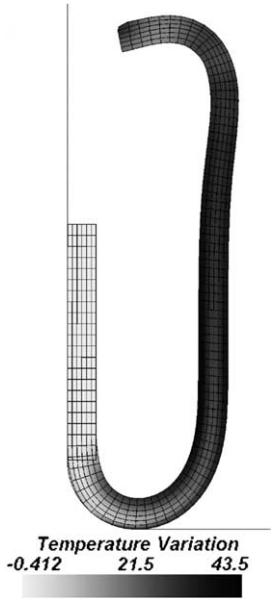

Fig. 38. Temperature fields—first order element—crushing at 55 km/h. Time: 3.273×10^{-3} s.

point out the evanescence of the oscillations. Let us also note that the final temperature distribution is very similar to the one resulting from the use of first order elements.

Fig. 43 shows the evolutions of the temperature at point A for both type of elements. For this crushing speed the peak temperature is clearly higher than for the process at 1 km/h, and also higher when using first

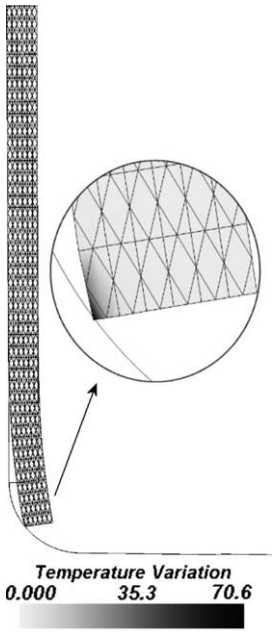

Fig. 39. Temperature fields—-mixed order element—crushing at 55 km/h. Time: 1.636×10^{-4} s.

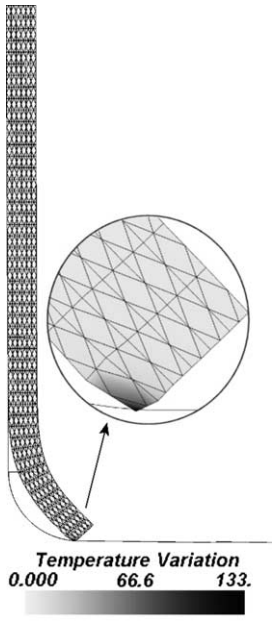

Fig. 40. Temperature fields—-mixed order element—crushing at 55 km/h. Time: 3.273×10^{-4} s.

order thermal elements rather than second order thermal elements (for the same reasons as before). It is important to point out that, in this case, this last difference is also due to an overestimation of the peak

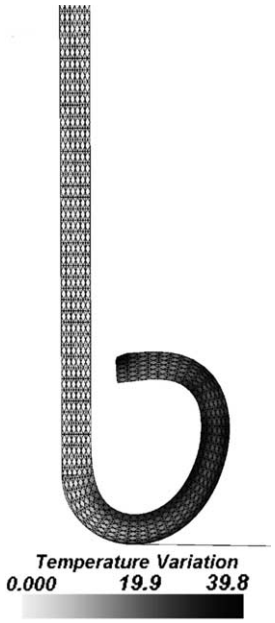

Fig. 41. Temperature fields—-mixed order element—crushing at 55 km/h. Time: 1.636×10^{-3} s.

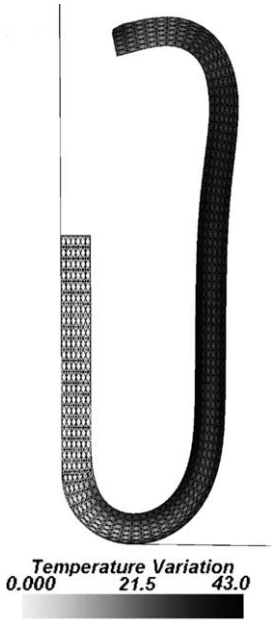

Fig. 42. Temperature fields—-mixed order element—crushing at 55 km/h. Time: 3.273×10^{-3} s.

temperature by the first order thermal element resulting from the 'skin effect'. The final temperature at point A asymptotically tends to be close to the one given by the 1 km/h crushing model.

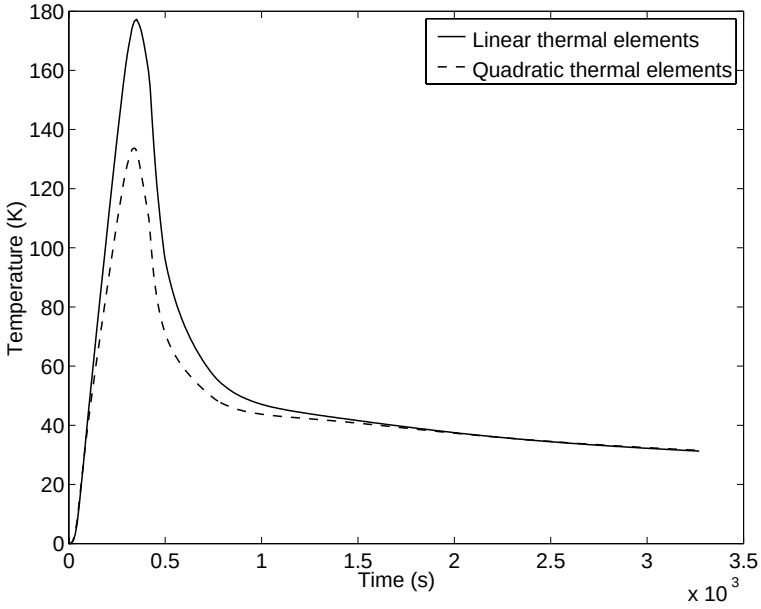

Fig. 43. Evolution of the temperature at point A—crushing at 55 km/h.

The evolution of the crushing force is drawn in Fig. 44 for various cases. We can notice that the increase in crushing speed, which induces a decrease of the frictional interactions, leads to a more important decrease of the apparent strength of the tube.

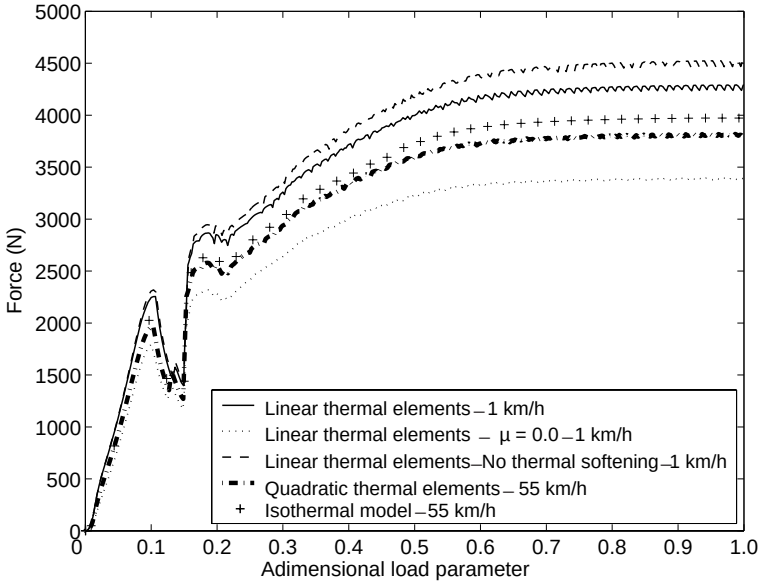

Fig. 44. Evolution of the crushing force (by unit hoop angle)—crushing at 55 km/h.

For this application, the oscillatory behavior observed in the temperature field for the first order elements does not affect the evolution of the crushing force. Indeed, the average temperature in the continuum, and thus the mean resistance, is not modified by the oscillations in the temperature field. This last remark does not justify the use of mesh or elements that results in an oscillatory behavior of the predictions. Thus, the use of mixed order elements, based on first order mechanical elements and quadratic thermal elements, enables us to obtain much more accurate results without increasing the number of mechanical degrees of freedom.

7. Conclusions

A complete thermomechanical formalism at finite strains was developed to model processes such as metal forming or impact of structures. Concerning the finite element formalism we were interested in two approaches: the classical Selective Reduced Integration (SRI) and the less classical Enhanced Assumed Strain (EAS). These techniques enable the suppression of the volumetric and/or the shear locking. As expected, the use of the EAS enhancement delivers better results in the case of large shear deformations and exhibits a better coarse mesh accuracy. This situation appears here through the buckling of a cylinder, but can also appear through shear banding (see Adam, 2003; Steinmann and Willam, 1991).

As exposed by Glaser and Armero (1997), hourglassing problems in the EAS formulation can develop but the use, as in the present work, of an Updated Enhanced Lagrangian approach pushes aside the apparition of such mesh instabilities. The tangent operator in this Updated Lagrangian framework was derived using the consistent tangent operator developed in Ponthot (2002) for the hypoelastic constitutive formulation under consideration.

The choice of a purely local scheme of solution of the EAS modes simplifies the introduction of such formulation in an existing thermomechanical finite element code, and produces little CPU increase when used for large models.

We have also exposed the use of mixed order finite elements based on first order mechanical and second order thermal shape functions. These are of special interest to capture huge thermal gradients without being obliged to refine both the mechanical and thermal discretization. Thus, coupling the coarse mesh accuracy of the EAS formalism with quadratic thermal elements can be helpful for large models where a fine discretization cannot be made.

References

Adam, L., 2003. Modélisation du comportement thermo-élasto-viscoplastique des métaux soumis á grandes déformations. Application au formage superplastique. Ph.D. thesis, Université de Liège.

Adam, L., Ponthot, J., 2002a. Numerical simulation of viscoplastic and frictional heating during finite deformation of metal—Part 1: Theory. ASCE-Journal of Engineering Mechanics 128 (11), 1215–1221.

Adam, L., Ponthot, J., 2002b. Numerical simulation of viscoplastic and frictional heating during finite deformation of metal—Part 2: Applications. ASCE-Journal of Engineering Mechanics 128 (11), 1222–1232.

Andelfinger, U., Ramm, E., 1993. EAS-elements for two-dimensional and three-dimensional, plate and shell structures and their equivalence to hr-elements. International Journal of Numerical Methods in Engineering 36, 1311–1337.

Argyris, J., Doltsinis, J., 1981. On the natural formulation and analysis of large deformation coupled thermomechanical problems. Computer Methods in Applied Mechanics and Engineering 25, 195–253.

Arif, A., Pervez, T., Mughal, M., 2000. Performance of finite element procedure for hyperelastic–viscoplastic large deformation problem. Finite Elements in Analysis and Design 34, 89–112.

Armero, F., Simo, J., 1992. A new unconditionally stable fractional step method for non-linear coupled thermomechanical problem. International Journal of Numerical Methods in Engineering 35, 737–766.

Armero, F., Simo, J., 1993. A priori estimates and unconditionally stable product formula algorithms for nonlinear coupled thermoplasticity. International Journal of Plasticity 9, 749–782.

Bathe, K.-J., 1996. Finite Element Procedures. Prentice Hall Edition, Englewood Cliffs, NJ.

Beltran, F., Goicolea, J., 1989. Large strain plastic collapse: A comparison of explicit and implicit solutions. In: Owen, D., Hinton, E., Oñate, E. (Eds.), International Conference on Computational Plasticity (COMPLAS 2). Pineridge Press, Barcelona, Spain, pp. 1125–1136.

Booley, B., Weiner, J., 1960. Theory of Thermal Stresses. Wiley.

Brezzi, F., Fortin, M., 1991. Mixed and Hybrid Finite Element Methods. Springer, New-York.

Camacho, G., Ortiz, M., 1997. Adaptative Lagrangian modeling of ballistic penetration of metallic targets. Computer Methods in Applied Mechanics and Engineering 60, 813–821.

Chrysochoos, A., 1987. The heat evolved during an elastic–plastic transformation at finite strains. In: Bui, H., Nguyen, Q. (Eds.), Thermomechanical Couplings in Solids. IUTAM.

Chrysochoos, A., Louche, H., 2000. An infrared image processing to analyse the calorific effects accompanying strain localization. International Journal of Engineering Science 38, 1759–1788.

de Souza Neto, E., Peric, D., 1995. Remarks on the stability of enhanced strain elements in finite elasticity and elastoplasticity. Communications in Numerical Methods in Engineering 11, 951–961.

Flanagan, D., Belytschko, T., 1981. A uniform strain hexahedron and quadrilateral with orthogonal hourglass control. International Journal of Numerical Methods in Engineering 17, 679–706.

Garcia Garino, C., 1993. Un modelo numerico para el analysis de solidos elastoplasticos sometidos a grandes deformaciones. Ph.D. thesis, UPC, Barcelona.

Glaser, S., Armero, F., 1997. On the formulation of enhanced strain finite elements in finite deformations. Engineering Computations 14 (7), 759–791.

Hansbo, P., 1998. A new approach to quadrature for finite elements incorporating hourglass control as a special case. Computer Methods in Applied Mechanics and Engineering 158, 301–309.

Hogge, M., 1977. Integration operators for first order linear matrix differential equations. Computer Methods in Applied Mechanics and Engineering 11, 281–294.

Hugues, T., 1977. Unconditionally stable algorithms for nonlinear heat conduction. Computer Methods in Applied Mechanics and Engineering 10, 135–139.

Ibrahimbegovic, A., Chorfi, L., 2002. Covariant principal axis formulation of associated coupled thermoplasticity at finite strains and its numerical implementation. International Journal of Solids and Structures 39, 499–528.

Laursen, T., 1992. Formulation and treatment of frictional contact problems using finite elements. Ph.D. thesis, Department of Mechanical Engineering, Stanford University.

Laursen, T., 2002. Computational Contact and Impact Mechanics. Fundamentals of Modeling Interfacial Phenomena in Nonlinear Finite Element Analysis. Springer, New-York.

Lehmann, T., 1984. CISM courses and lectures 281. CISM, Ch. The constitutive laws in thermoplasticity.

Lemaitre, J., Chaboche, J.-L., 1985. Mécanique Des Matériaux Solides. Dunod.

Lion, A., 2000. Constitutive modelling in finite thermoviscoplasticity: a physical approach based on nonlinear rheological models. International Journal of Plasticity 16, 469–494.

Malkus, D., Hughes, T., 1978. Mixed finite element methods—reduced and selective integration techniques: a unification of concepts. Computer Methods in Applied Mechanics and Engineering 15, 63–81.

Malvern, L., 1969. Introduction to the Mechanics of Continuous Medium. Prentice-Hall.

Ponthot, J., 1995. Traitement unifié de la mécanique des milieux continus solides en grandes transformations par la méthode des éléments finis. Ph.D. thesis, University of Liège, Liège, Belgium.

Ponthot, J., 2002. Unified stress update algorithms for the numerical simulation of large deformation elasto-plastic and elasto-viscoplastic processes. International Journal of Plasticity 18, 91–126.

Reese, S., Wriggers, P., Reddy, B., 2000. A new locking-free brick element technique for large deformation problems in elasticity. Computers & Structures 75, 291–304.

Roehl, D., Ramm, E., 1996. Large elasto-plastic finite element analysis of solids and shells with the enhanced assumed strain concept. International Journal of Solids and Structures 33 (20–22), 3215–3237.

Rosakis, P., Rosakis, A., Ravichandran, G., Hodowany, J., 2000. A thermodynamic internal variable model for the partition of plastic work into heat and stored energy in metals. Journal of Mechanics and Physics of Solids 48, 581–607.

Simo, J., 1985. On the computational significance of the intermediate configuration and hyperelastic stress relations in finite deformation elasto-plasticity. Mechanics of Materials 4, 439–451.

Simo, J., Armero, F., 1992. Geometrically non-linear enhanced strain mixed methods and the method of incompatible modes. International Journal of Numerical Methods in Engineering 33, 1413–1449.

Simo, J., Hughes, T., 1987. General return mapping algorithms for rate independent plasticity. In: Constitutive Laws for Engineering Materials: Theory and Applications. Elsevier Science Publishing Co.

Simo, J., Miehe, C., 1992. Associative coupled thermoplasticity at finite strains: Formulation, numerical analysis and implementation. Computer Methods in Applied Mechanics and Engineering 98, 41–104.

Simo, J., Rifai, M., 1990. A class of mixed assumed strain methods and the methods of incompatible modes. International Journal of Numerical Methods in Engineering 29, 1595–1638.

Simo, J., Armero, F., Taylor, R., 1993. Improved versions of assumed enhanced strain tri-linear elements for 3D finite deformation problems. Computer Methods in Applied Mechanics and Engineering 110, 359–386.

Steinmann, P., Willam, K., 1991. Performance of enhanced finite element formulation in localized failure computations. Computer Methods in Applied Mechanics and Engineering 90, 845–867.

Svendsen, B., Arndt, S., Klingbeil, D.R.S., 1998. Hyperelastic models for elastoplasticity with non-linear isotropic and kinematic hardening at large deformation. International Journal of Solids and Structures 35 (25), 3363–3389.

Taylor, G., Quinney, H., 1937. The latent heat remaining in a metal after cold work. Proceedings of The Royal Society (London) A163, 157–181.

Tonkovic, Z., Soric, J., Kratzig, W., 2001. On nonisothermal elastoplastic analysis of shell components employing realistic hardening responses. International Journal of Solids and Structures 38, 5019–5039.

Wall, W., Bischoff, M., Ramm, E., 2000. A deformation dependent stabilization technique, exemplified by EAS elements at large strains. Computer Methods in Applied Mechanics and Engineering 188, 859–871.

Weber, G., Anand, L., 1990. Finite deformation constitutive equations and a time integration procedure for isotropic, hyperelastic–viscoplastic solids. Computer Methods in Applied Mechanics and Engineering 79, 173–202.

Whertheimer, T., 1982. Thermal mechanically analysis in metal forming processes. In: Pittman, Wood, Alexander, Zienkiewicz (Eds.), Numerical Methods in Industrial Forming Processes. Swansea, UK, pp. 425–434.

Wriggers, P., 2002. Computational Contact Mechanics. Wiley.

Wriggers, P., Miehe, C., Kleiber, M., Simo, J., 1989. On the coupled thermomechanical treatment of necking problems via FEM. In: Owen, D., Hinton, E., Oñate, E. (Eds.), International Conference on Computational Plasticity (COMPLAS 2). Pineridge Press, Barcelona, Spain, pp. 527–542.

Zhong, Z., 1993. Finite Element Procedures for Contact Impact Problems. Oxford Sciences Publications.

Zhou, M., Rachivadran, G., Rosakis, A., 1996. Dynamically propagating shear bands in impact-loaded prenotched plates—II: Numerical simulations. Journal of Mechanics and Physics of Solids 44, 1007–1032.

Zienkiewicz, O., Taylor, R., 1994. The Finite Element Method, vol. 1. McGraw-Hill.